

RESEARCH ARTICLE

10.1002/2017GB005671

Key Points:

- A new parameterization for marine N_2O production by nitrification and denitrification is developed
- Modern marine N_2O emissions are constrained by observations to 4.3 (2.8 to 5.9) $Tg\ N\ yr^{-1}$
- Probabilistic projections yield massive reductions in O_2 and a long-term increase in N_2O emissions

Correspondence to:

G. Battaglia,
battaglia@climate.unibe.ch

Citation:

Battaglia, G., & Joos, F. (2018). Marine N_2O emissions from nitrification and denitrification constrained by modern observations and projected in multimillennial global warming simulations. *Global Biogeochemical Cycles*, 32. <https://doi.org/10.1002/2017GB005671>

Received 17 MAR 2017

Accepted 11 DEC 2017

Accepted article online 16 DEC 2017

Marine N_2O Emissions From Nitrification and Denitrification Constrained by Modern Observations and Projected in Multimillennial Global Warming Simulations

G. Battaglia^{1,2} and F. Joos^{1,2}
¹Climate and Environmental Physics, Physics Institute, University of Bern, Bern, Switzerland, ²Oeschger Centre for Climate Change Research, University of Bern, Bern, Switzerland

Abstract Nitrous oxide (N_2O) is a potent greenhouse gas (GHG) and ozone destructing agent; yet global estimates of N_2O emissions are uncertain. Marine N_2O stems from nitrification and denitrification processes which depend on organic matter cycling and dissolved oxygen (O_2). We introduce N_2O as an obligate intermediate product of denitrification and as an O_2 -dependent by-product from nitrification in the Bern3D ocean model. A large model ensemble is used to probabilistically constrain modern and to project marine N_2O production for a low (Representative Concentration Pathway (RCP)2.6) and high GHG (RCP8.5) scenario extended to A.D. 10,000. Water column N_2O and surface ocean partial pressure N_2O data serve as constraints in this Bayesian framework. The constrained median for modern N_2O production is 4.5 ($\pm 1\sigma$ range: 3.0 to 6.1) $Tg\ N\ yr^{-1}$, where 4.5% stems from denitrification. Modeled denitrification is 65.1 (40.9 to 91.6) $Tg\ N\ yr^{-1}$, well within current estimates. For high GHG forcing, N_2O production decreases by 7.7% over this century due to decreasing organic matter export and remineralization. Thereafter, production increases slowly by 21% due to widespread deoxygenation and high remineralization. Deoxygenation peaks in two millennia, and the global O_2 inventory is reduced by a factor of 2 compared to today. Net denitrification is responsible for 7.8% of the long-term increase in N_2O production. On millennial timescales, marine N_2O emissions constitute a small, positive feedback to climate change. Our simulations reveal tight coupling between the marine carbon cycle, O_2 , N_2O , and climate.

1. Introduction

Nitrous oxide (N_2O) is an atmospheric trace gas that plays important roles in the stratospheric ozone cycle and as a greenhouse gas (GHG) that is more than 200 times more potent than carbon dioxide (CO_2) (Gruber, 2008). Natural N_2O emissions to the atmosphere result from microbial metabolic pathways on land and in the oceans. N_2O is inert within the troposphere and is photochemically decomposed after mixing into the stratosphere. Prather et al. (2015) suggest that the preindustrial atmospheric lifetime of N_2O was 123 years, which constrains natural N_2O sources to $10.5 \pm 1\ Tg\ N\ yr^{-1}$. Measurements of N_2O concentration ($[N_2O]$) and N_2O production and reduction rates in natural settings are difficult and sparse which makes the attribution of N_2O sources and sinks to processes and systems uncertain. Estimates of global terrestrial and oceanic N_2O emissions from natural sources vary by up to a factor of 5. They range between 3.3 and 9.0 $Tg\ N\ yr^{-1}$ and between 1.8 and 9.45 $Tg\ N\ yr^{-1}$ for terrestrial and oceanic emissions, respectively (Ciais et al., 2013). During the last 100 years, atmospheric N_2O concentrations have increased from ~ 270 ppb currently reaching ~ 325 ppb as result of additional, anthropogenic sources (2.7–11.1 $Tg\ N\ yr^{-1}$, Ciais et al., 2013).

Hot spot regions for marine N_2O production are the low oxygenated waters of the eastern boundary upwelling systems, such as the Arabian Sea (Law & Owens, 1990; Naqvi et al., 2000; Nicholls et al., 2007), the southern African coast (Frame et al., 2014), and the eastern equatorial Pacific (Arévalo-Martínez et al., 2016, 2015; Babbín et al., 2015; Ji et al., 2015; Kock et al., 2016; Zamora et al., 2012). N_2O production also occurs in well-oxygenated waters. Most studies associate N_2O production with processes in the open ocean water column. In coastal environments, however, N_2O might also be produced from interactions with sediments (Frame et al., 2014).

In the ocean, N_2O primarily forms (i) as a by-product from nitrification and (ii) as an intermediate product from respiratory denitrification. Process-oriented studies measure water column concentrations of involved species, incubate water samples with isotopes, determine the N_2O isotopomer configuration or probe

relevant genomes or enzymes. The exact metabolic pathways and their relative importance for global N_2O production remain unclear as is the future evolution of marine N_2O emissions (Bange, 2008; Freing et al., 2012). Both nitrification and denitrification processes and the related N_2O production are tightly linked to the cycling of organic matter and oxygen concentrations ($[\text{O}_2]$).

Nitrification by autotrophs occurs nearly everywhere in the global ocean where organic matter is remineralized aerobically releasing ammonia (NH_3). Nitrification is a two-step process, whereby NH_3 is first oxidized to nitrite (NO_2^-) by ammonia-oxidizing archaea (AOA) or ammonia-oxidizing bacteria (AOB), and subsequently, NO_2^- is oxidized to nitrate (NO_3^-) by nitrite-oxidizing bacteria. Both reactions are linked to the reduction of O_2 . N_2O has been reported as secondary product from ammonia oxidation (Goreau et al., 1980; Ji et al., 2015; Loescher et al., 2012; Nevison, 2003; Ward, 2008), though the relevance of different biogeochemical pathways remains somewhat controversial. N_2O can form from NH_3 oxidation to NO_2^- by AOA and AOB. In addition, AOA (Santoro et al., 2011) and AOB (Frame & Casciotti, 2010) have been shown to also be able to reduce NO_2^- to N_2O in laboratory cultures through pathways similar to those involved in heterotrophic denitrifiers, a process also referred to as nitrifier denitrification. Microenvironments within sinking particles may provide favorable conditions, that is, low $[\text{O}_2]$ and availability of organic carbon (Breider et al., 2015; Charpentier et al., 2007; Frame et al., 2014; Popp et al., 2002; Wilson et al., 2014). Isotopic constraints suggest that AOA might well dominate local and global nitrification and N_2O production (Beman et al., 2012; Francis et al., 2005; Loescher et al., 2012; Peng et al., 2015; Santoro et al., 2011; Trimmer et al., 2016) and also be active in the euphotic zone, where AOB are thought to be light inhibited (Ward, 2008). Several studies inferred surface production of N_2O (Charpentier et al., 2010; Dore & Karl, 1996; Law & Ling, 2001; Morell et al., 2001), but the global relevance of N_2O production in the euphotic zone is debated (Freing et al., 2012; Zamora & Oschlies, 2014).

Respiratory denitrification occurs under anoxic conditions, and N_2O is formed as an intermediary product. A series of nitrogen oxide compounds are used as terminal electron acceptors for the oxidation of organic matter in the absence of O_2 which ultimately produces N_2 ($\text{NO}_3^- \rightarrow \text{NO}_2^- \rightarrow \text{NO} \rightarrow \text{N}_2\text{O} \rightarrow \text{N}_2$). The net N_2O production results from potentially large gross fluxes of production and consumption (Bange, 2008; Devol, 2008). The different denitrification steps have been shown to exhibit different O_2 sensitivities, with N_2O production starting at higher $[\text{O}_2]$ compared to N_2O reduction (Babbin et al., 2015; Castro-Gonzalez & Farias, 2004; Ji et al., 2015). Resulting N_2O depth profiles may exhibit characteristic double peak structure, where N_2O is depleted within anoxic zones (Arévalo-Martínez et al., 2016; Babbin et al., 2015; Bange, 2008; Ji et al., 2015; Kock et al., 2016). Nitrification and denitrification share common intermediate products (NO_2^- , N_2O) such that processes are potentially coupled at suboxic transitions within the water column complicating the interpretation of in situ profile data (Devol, 2008; Frame et al., 2014; Ji et al., 2015).

Additional processes such as heterotrophic nitrification (Bange, 2008), anammox (Kartal et al., 2007), and chemoautotrophic denitrification (Gilly et al., 2013) might also contribute to N_2O production. It has also been suggested that an interplay of abiotic-biotic reactions might lead to N_2O production, where enzymatically produced intermediates (NH_2OH , NO_2^-) are oxidized or reduced to N_2O by metals (Zhu-Barker et al., 2015).

Given these complexities, modeling studies so far have largely employed highly parameterized frameworks and do not resolve the mentioned intermediate products or individual process rates. Studies have estimated global marine N_2O emissions either from interpolated surface measurements of pN_2O and related air-sea flux parameterizations ($4 (1.2\text{--}6.8) \text{ Tg N yr}^{-1}$ Nevison et al., 1995) or from inferred N_2O yields per O_2 consumption coupled to observed O_2 or temperature climatologies and modeled or observationally inferred respiration rates ($5.8 \pm 2 \text{ Tg N yr}^{-1}$ Nevison, 2003, $2.2\text{--}4.3 \text{ Tg N yr}^{-1}$ Freing et al., 2012, and $6.2 \pm 3.2 \text{ Tg N yr}^{-1}$ Bianchi et al., 2012). Modeling studies within global ocean circulation models usually couple N_2O production to modeled aerobic remineralization fluxes, assuming that nitrification follows aerobic remineralization instantaneously. The yield of N_2O per unit organic matter remineralized is assumed to depend nonlinearly (Schmittner et al., 2009; Suntharalingam & Sarmiento, 2000) or linearly (Zamora et al., 2012; Zamora & Oschlies, 2014) on oxygen concentrations. Sometimes a first-order (Jin & Gruber, 2003; Martinez-Rey et al., 2015) or zeroth-order (Zamora & Oschlies, 2014) consumption term for denitrification is included. The $[\text{O}_2]$ threshold below which consumption starts is different in different models ($10 \text{ mmol m}^{-3} \text{ O}_2$, Zamora et al., 2012, 4 mmol m^{-3} , Nevison, 2003; Jin & Gruber, 2003, and 5 mmol m^{-3} , Martinez-Rey et al., 2015).

Explicit N_2O production and consumption from denitrification in line with requirements from organic matter stoichiometry and with O_2 -dependent decoupling of N_2O production and consumption was only recently implemented in a 1-D water column model (Babbin et al., 2015). This model was applied together with

observations of N_2O and related tracers in the eastern tropical North Pacific (Babbin et al., 2015), and denitrification was identified as the major net source of N_2O . Trimmer et al. (2016), on the other hand, employing a similar model, explained their data from a neighboring site with low oxygen archaeal production from nitrification. N_2O production in this study was modeled as an exponential function of $-\text{[O}_2\text{]}$, without coupling to remineralization rates. Nevertheless, results by Ji et al. (2015) and Babbin et al. (2015) confirm that gross local N_2O fluxes from denitrification may be up to hundred times larger than those from nitrification. Yet gross fluxes from denitrification, consistently linked to the stoichiometry of organic matter fluxes, have never been implemented in a global ocean circulation model.

Here in a novel approach, we implement marine N_2O production and consumption fluxes within the Bern3D Earth System Model of Intermediate Complexity (EMIC). Stoichiometric relationships between the produced and consumed N_2O from denitrification and their corresponding organic matter fluxes are explicitly considered. We interpret modeled mean O_2 concentrations in each grid cell to represent a range of $[\text{O}_2]$ and microenvironmental conditions at the subgrid scale. This is described by a distribution around the mean $[\text{O}_2]$ allowing nitrification and denitrification to co-occur within the same grid cell in low oxygen waters. Nitrification is modeled with an exponential O_2 -dependent yield from organic matter remineralization fluxes in line with earlier parameterizations. Denitrification considers stoichiometry with respect to organic matter fluxes following Paulmier et al. (2009) and a Michaelis-Menten-type regulation of N_2O consumption. N_2O is taken as the only obligate intermediate of the denitrification series. This permits us to evaluate simulated denitrification fluxes with independent estimates of total nitrogen (N) loss ($20\text{--}150\text{ Tg N yr}^{-1}$, as summarized in Yang & Gruber, 2016).

Model parameters and uncertainties are estimated in a Bayesian, Monte Carlo approach using a 1,000-member model ensemble. For the first time, both water column concentration and surface partial pressure N_2O data (Kock & Bange, 2015) are used together as constraints. In addition, the model circulation, simulated O_2 distribution, and remineralization fluxes are constrained by observation-derived fields of natural radiocarbon (Key et al., 2004) and dissolved O_2 (Bianchi et al., 2012; Garcia et al., 2014). Data-constrained, probabilistic estimates are presented for regional-to-global marine N_2O production and consumption, sea-to-air N_2O fluxes, and the marine N_2O -climate feedback. The simulations cover the industrial period and the 21st century applying a low (Representative Concentration Pathway (RCP)2.6) and a high (RCP8.5) greenhouse gas scenario. These are extended to year A.D. 10,000 to quantify century to millennial-scale changes and long-term feedbacks between marine N_2O and climate similar to the constant composition commitment simulations presented in Zickfeld et al. (2013).

2. Modeling Framework

2.1. The Bern3D Model

The Bern3D Earth System Model of Intermediate Complexity is a three-dimensional frictional geostrophic balance ocean model (Müller et al., 2006) with a sea ice component coupled to a single-layer energy and moisture balance model of the atmosphere (Ritz et al., 2011) and a prognostic marine biogeochemistry module (Parekh et al., 2008; Tschumi et al., 2011). Here a version with a horizontal resolution of 41 by 40 grid cells and 32 logarithmically scaled vertical layers is used (see also Battaglia et al., 2016; Roth et al., 2014). The components atmosphere, ocean, and sea ice share the same horizontal resolution. The physical ocean model has an isopycnal diffusion scheme and Gent-McWilliams parameterization for eddy-induced transport (Griffies, 1998). The National Centers for Environmental Prediction/National Center for Atmospheric Research monthly wind stress climatology (Kalnay et al., 1996) is prescribed at the surface. Air-sea gas exchange, carbonate chemistry, and natural $\Delta^{14}\text{C}$ of dissolved inorganic carbon are modeled according to Ocean-Carbon Cycle Model Intercomparison Project (OCMIP)-2 protocols (Najjar et al., 1999; Orr & Najjar, 1999). Carbonate chemistry calculations are updated according to Orr and Epitalon (2015). The global mean air-sea transfer rate is reduced by 19% compared to OCMIP-2 to match observation-based estimates of natural and bomb-produced radiocarbon (Müller et al., 2008). N_2O solubility and the Schmidt number are calculated according to Wanninkhof (1992).

The carbon cycle model (Parekh et al., 2008; Tschumi et al., 2011) simulates production and remineralization/dissolution of organic matter, calcium carbonate, and opal. The N cycle is not explicitly modeled. The euphotic zone is defined above 75 m. Production of particulate organic matter (POP, expressed in phosphorous (P) units) within the euphotic zone is a function of temperature, light availability, phosphate, and iron following Doney et al. (2006). Remineralization of POP follows a power law profile (Martin et al., 1987, equation (A1)). The organic flux reaching the seafloor is remineralized in the deepest box. As in the original

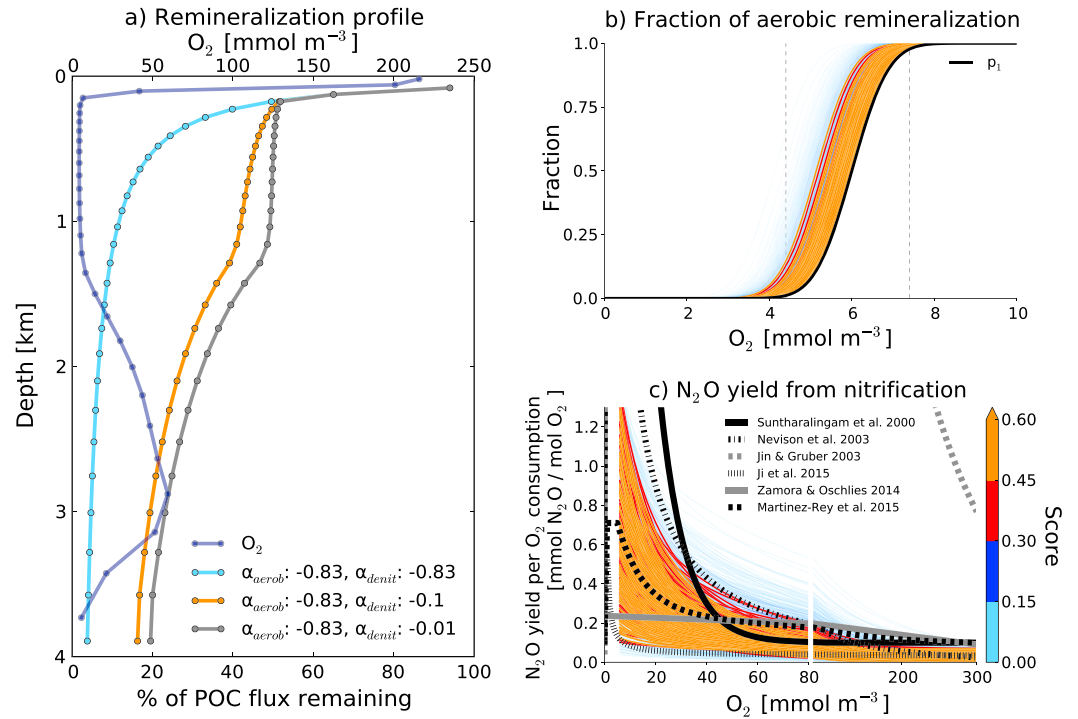


Figure 1. Remineralization profiles, fraction of aerobic remineralization, and N₂O yield factors. (a) The original remineralization profile using the standard value of α_{aerob} (light blue profile) and two profiles with lower remineralization under anaerobic conditions indicating the sampled range in α_{denit} (orange and gray profiles). (b) Fraction of aerobic remineralization p_1 as a function of grid cell mean-dissolved O₂ (black line). Colored lines offset to lower [O₂] represent the sampled p_2 distributions to regulate N₂O production and consumption by denitrification. Vertical dashed lines indicate the 2σ range of p_1 . (c) N₂O yield from nitrification as sampled in the Monte Carlo framework (colored lines). Black thick lines show N₂O yields from the literature. Colored lines in Figures 1b and 1c are coded according to the skill score of the related model simulation.

model version, two thirds of organic matter production form dissolved organic matter (DOP), which here decays into its mineral constituents with an e -folding lifetime of 1.5 years. A new formalism is introduced which assigns remineralization of POP and DOP to aerobic (p_1) and anaerobic ($1-p_1$) pathways depending on the mean grid cell-dissolved O₂ concentration (see p_1 in Figure 1b and equation (A5)). We introduce two power law profiles, F_{aerob} and F_{denit} , with two distinct remineralization length scales for aerobic and anaerobic remineralization (α_{aerob} and α_{denit}). The changes of the respective piecewise Martin curves are weighted with $p_1([O_2])$ and $(1-p_1([O_2]))$ to yield the total remineralization profile (equations (A2)–(A4)). This way, aerobic and anaerobic remineralization may co-occur within the same grid cell. The effect on the remineralization profile is illustrated in Figure 1a (refer to the Appendix A for implemented equations).

2.2. Marine N₂O Pathways

2.2.1. N₂O From Nitrification

Net nitrification is assumed to instantly follow aerobic remineralization and is stoichiometrically accounted for in the O₂ consumption term ($J(O_2)$; see equation (A6) (as equation 10 in Paulmier et al., 2009). N₂O produced during nitrification ($J(N_{2O_{nit.prod.}})$ (mmol N₂O m⁻³ s⁻¹) is therefore coupled to the aerobic remineralization flux below the euphotic zone with an O₂-dependent yield:

$$J(N_{2O_{nit.prod.}}) = [\alpha + \beta \cdot f([O_2])] \cdot J(O_2), \quad (1)$$

$$f([O_2]) = f_1 \cdot \exp(-f_2 \cdot [O_2]) + (1 - f_1) \cdot \exp(-f_3 \cdot [O_2]). \quad (2)$$

α is a constant yield factor (not to be confused with α_{aerob} and α_{denit}) and the function $\beta \cdot f(O_2)$ describes an O₂-dependent N₂O yield from nitrification (Figure 1c). This O₂-dependent yield of nitrification follows the functional form applied by Jin and Gruber (2003) and Martinez-Rey et al. (2015) using two exponentials (equation (2)). It is motivated by the linear relationship between excess N₂O and apparent oxygen utilization in well-oxygenated waters (Butler et al., 2000; Cohen & Gordon, 1979), laboratory data of Goreau et al. (1980),

oceanic observations of Nevison (2003) and Ji et al. (2015), and most recent incubation results of Trimmer et al. (2016). This functional form is chosen here as it offers many degrees of freedom and therefore produces a wide range of solutions; from almost linear to exponential covering the range reported by other studies. Parameterizations employed in other global modeling studies (Jin & Gruber, 2003; Martinez-Rey et al., 2015; Nevison, 2003; Suntharalingam et al., 2000; Zamora & Oschlies, 2014) and derived in observational studies (Ji et al., 2015) are shown in Figure 1c for comparison. N_2O production emerges from the product of yield and remineralization rate. The selected range of parameterizations covers the parameterizations used by Nevison (2003), Zamora and Oschlies (2014), and Martinez-Rey et al. (2015), whereas Jin and Gruber (2003) used a similar functional form but applied much higher yield factors. This discrepancy was also noted in Martinez-Rey et al. (2015, section 2.2, p. 4136) and could arise from lower remineralization fluxes in the low O_2 regions in the Jin and Gruber (2003) model.

2.2.2. N_2O From Denitrification

N_2O consumption from denitrification is modeled with first-order kinetics following Yamagishi et al. (2007) and Babbin et al. (2015), and consumption is therefore the product of a loss rate k_c and $[\text{N}_2\text{O}]$. To ease notation, grid cell indices (x, y, k) are omitted. In addition, a Michaelis-Menten term reduces the consumption rate coefficient, k_c , at low $[\text{N}_2\text{O}]$ and a function $(1-p_2)$ describes the grid cell fraction with consumption. k_c (in units of s^{-1}) equals

$$k_c = \frac{1}{\tau} \cdot \frac{[\text{N}_2\text{O}]}{K_{\text{N}_2\text{O}} + [\text{N}_2\text{O}]} \cdot (1 - p_2). \quad (3)$$

We introduce a function, p_2 (Figure 1b), as a function of the mean grid cell $[\text{O}_2]$ to parameterize small-scale processes of N_2O consumption and production. p_2 codetermines the relative importance of N_2O consumption and N_2O production by denitrification (see equation (B1) and Figure 1b). This way, N_2O consumption by denitrification sets in at lower $[\text{O}_2]$ compared to N_2O production by denitrification in agreement with observations (Babbin et al., 2015; Castro-Gonzalez & Farias, 2004; Ji et al., 2015) and similar to the 1-D water column model of Babbin et al. (2015). Potential N_2O consumption by denitrification is computed by using a semiimplicit numerical scheme as the timescale for consumption ($1/k_c$) is a few days only and comparable to the length of the model time step, Δt

$$J(\text{N}_2\text{O}_{\text{denit. cons.}})^{\text{pot}} = -k_c \cdot [\text{N}_2\text{O}] \frac{1}{(1 + \Delta t \cdot k_c)},$$

where the fraction results from the numerical scheme.

Potential N_2O consumption rates do not depend on organic matter availability and may thus exceed corresponding organic matter conversion rates. This would violate the first-order principle of mass conservation. In addition, N_2O production by denitrification is assumed to co-occur in low oxygen grid cells which is also coupled to anaerobic remineralization of organic matter. Therefore, we limit N_2O consumption, $J(\text{N}_2\text{O}_{\text{denit. cons.}})$ ($\text{mmol N}_2\text{O m}^{-3} \text{ s}^{-1}$) (i) by the anaerobic remineralization flux to conserve mass and (ii) by limiting the fraction of the anaerobic remineralization that is available for N_2O consumption to enforce that consumption and production can co-occur in a grid cell. We write

$$J(\text{N}_2\text{O}_{\text{denit. cons.}}) = -\min \left(k_c \cdot [\text{N}_2\text{O}] \frac{1}{(1 + \Delta t \cdot k_c)}, z_{\text{cons}} \cdot J_{\text{denit}}(\text{PO}_4) \cdot 20.5\% \right). \quad (4)$$

The first term in the minimum function represents potential N_2O consumption. The second term represents the upper limit of consumption as a function of anaerobic remineralization; $J_{\text{denit}}(\text{PO}_4)$ ($\text{mmol P m}^{-3} \text{ s}^{-1}$) is the P release from organic matter by denitrification ($\frac{\Delta F_{\text{denit}}(z_k)}{(z_{k-1} - z_k)} + \frac{|\text{DOP}| \cdot (1 - p_1)}{1.5 \text{ years}}$) and z_{cons} the stoichiometric ratio between P and N_2O for consumption (refer to the Appendix C for stoichiometric relationships, equation (C3)). The stoichiometric ratio for production ($z_{\text{source}} = 69$) is 4 times smaller than for consumption ($z_{\text{cons}} = 276$). Equal N_2O consumption and production by denitrification would therefore correspond to a share of $J_{\text{denit}}(\text{PO}_4)$ equal to 20% for N_2O consumption and equal to 80% for N_2O production. Here an upper limit share of 20.5% is applied for the N_2O consumption pathway in equation (4). This means that up to 5% more N_2O may be consumed than produced by denitrification within a grid cell. This choice permits a large range of consumption and production fluxes in our probabilistic approach, discussed in the next section, and reflects the notion that denitrification leads to a substantial net production not to a net consumption of N_2O (Babbin et al., 2015; Naqvi et al., 2000; Nicholls et al., 2007). In a small ensemble without the 20.5% limitation, consumption fluxes

Table 1
Sampled Model Parameters and Their Prior Distributions

Parameter	Description	Prior distribution ^a	Best consistent parameter set ^b
<i>Ocean transport and mixing</i>			
$k_{\text{diff-dia}}$	Ocean diapycnal diffusivity ($\text{m}^2 \text{s}^{-1}$)	$L(2.25\text{E}-5, s = 0.2, l = 0)$	$2.2\text{E}-05$
<i>Organic matter remineralization</i>			
α_{aerob}	Coefficient of Martin curve for aerobic remineralization	$N(-0.83, -0.0625)$	-0.83
α_{denit}	Coefficient of Martin curve for denitrification	$U(-0.1, -0.01)$	-0.03
<i>Nitrification</i>			
α	Background N_2O yield from nitrification ($\text{mol N}_2\text{O} / \text{mol O}_2$)	$U(0, 7\text{E}-5)$	$3.3\text{E}-05$
β	Maximal N_2O yield from nitrification at lowest $[\text{O}_2]$ ($\text{mol N}_2\text{O} / \text{mol O}_2$)	$U(5\text{E}-5, 2\text{E}-3)$	$9.1\text{E}-4$
f_1	Factor to weight first exponential in N_2O yield from nitrification	$U(0.4, 0.7)$	0.6
f_2^c	Rate of decrease in first exponential of N_2O yield from nitrification ($\text{m}^3 / \text{mol O}_2$)	$U(-150, -80)$	-83
f_3^c	Rate of decrease in second exponential of N_2O yield from nitrification ($\text{m}^3 / \text{mol O}_2$)	$U(-40, -10)$ $U(-40, -10)$	-25.5 -25.5
<i>Denitrification</i>			
τ	Timescale of N_2O consumption from denitrification (days)	$U(4, 20.9)$	10.5
$K_{\text{N}_2\text{O}}$	$[\text{N}_2\text{O}]$ where consumption rate is half its maximal value (Michaelis-Menten term) ($\mu\text{mol N}_2\text{O m}^{-3}$)	$U(10, 60)$	38.1
Offset	Offset in error function for N_2O consumption ($\text{mmol O}_2 \text{m}^{-3}$) (sampled around 0, absolute value is taken for model)	$N(0, 0.5)$	0.16

^aNormal distribution N (standard value, standard deviation), lognormal distribution L (standard value, s = shape parameter, l = location parameter), uniform distribution U (min., max.). ^bSee section 3.3; parameter set reproduces median fluxes and median concentration fields. ^cWe sampled f_2 and f_3 but give here also the ranges for their inverse values for convenience. The range in f_2 corresponds to a range in $(1/f_2)$ from 6.667 to 12.5 mmol m^{-3} . The range in f_3 corresponds to a range in $(1/f_3)$ from 25 to 100 mmol m^{-3} .

were slightly bigger decreasing net N_2O production by between $0.1\text{--}0.8 \text{ Tg N yr}^{-1}$. While the impact on emissions is small, the resulting N_2O concentrations show larger discrepancy with observations (higher errors and lower correlation).

The remaining remineralization of phosphorous is scaled to result in N_2O production ($\text{mmol N}_2\text{O m}^{-3} \text{s}^{-1}$):

$$J(\text{N}_2\text{O}_{\text{denit. prod.}}) = z_{\text{source}} \cdot \max \left(J_{\text{denit}}(\text{PO}_4) - \frac{|J(\text{N}_2\text{O}_{\text{denit. cons.}})|}{z_{\text{cons}}}, 0 \right). \quad (5)$$

Observations do not indicate large $[\text{N}_2\text{O}]$ gradients near the seafloor of the open ocean. Guided by this observation, the organic matter flux reaching the seafloor is not coupled to denitrification fluxes and N_2O production/consumption by denitrification is set to zero for this deposition flux. In other words, we implicitly postulate that organic matter reaching the seafloor is largely converted within reactive sediments and that any N_2O produced within the reactive sediment layer by denitrification is also consumed in these low oxygen environments. The overestimation of $[\text{N}_2\text{O}]$ in parts of the deep ocean (Figure 6) may be linked to these simplified boundary assumptions regarding nitrification and denitrification. To this end, we tested the impact on global N_2O production of our assumption of zero net production by denitrification near the seafloor in a sensitivity simulation using the “best consistent” parameter set shown in Table 1. Inclusion of N_2O production

and consumption by denitrification from the deposition flux in the lowermost cells leads to an increase in net N_2O production of 0.5 Tg N yr^{-1} . Then, simulated concentrations are higher leading to higher errors with available observations.

The Michaelis-Menten formalism and limiting the N_2O consumption to 20.5% of the anaerobic remineralization flux help to avoid that $[\text{N}_2\text{O}]$ falls below the saturation concentration. This would be in disagreement with available observations. The parameterization allows for large production and consumption fluxes of N_2O and potentially large net positive N_2O production from denitrification as argued for by Babbin et al. (2015). In addition, our parameterization considers appropriate stoichiometric ratios and ensures mass conservation such that organic matter is consumed only once. Mass conservation is usually neglected in 1-D studies (Babbin et al., 2015) but important for global applications. N_2O production and consumption at low O_2 concentrations in previous global studies was not explicitly tied to denitrification fluxes. The O_2 -dependent nitrification yield was sometimes taken to represent N_2O production from denitrification (Jin & Gruber, 2003; Martinez-Rey et al., 2015). For N_2O consumption, low rates were chosen ($\tau = 4$ months, Jin & Gruber, 2003, $k^{-1} = (1/0.138)$ years = 7.2 years Martinez-Rey et al., 2015) or assumed to follow zero-order kinetics (Zamora & Oschlies, 2014).

2.3. Ensemble Generation, Metrics for Skill Assessment, and Data Sets

Latin hypercube sampling (McKay et al., 1979) is applied to generate a 1,000-member ensemble including 11 parameters (Table 1). It is an efficient, statistical, Monte Carlo sampling technique which generates controlled random samples from a multidimensional distribution. The sampled parameters concern ocean transport and mixing (one parameter) and organic matter remineralization (two parameters) as these exert a crucial control on N_2O production. Importantly, the parameters governing the N_2O yield from nitrification (five parameters) and parameters affecting N_2O consumption by denitrification (three parameters) are sampled. We apply normal, uniform, or lognormal priors based on literature information and previous sensitivity tests (see below and Table 1). Normal or lognormal distributions are chosen if a best guess parameter value has previously been identified (α_{aerob} , $k_{\text{diff-dia}}$, offset). Lognormal distributions are chosen for asymmetric ranges to limit the parameter values at the lower range. Uniform distributions are chosen for parameters which are poorly known. For each ensemble member and each of the data sets (see below) a relative mean square error (MSE^{rel}) is calculated as a sum over all grid cells (indexed j) where observations are available. The sum is weighted by a_j , which represents the grid cell volume/area and normalized by σ^2 :

$$\text{MSE}^{\text{rel}} = \sum_j a_j \cdot \frac{(\chi_j^{\text{model}} - \chi_j^{\text{obs}})^2}{\sigma^2}. \quad (6)$$

Model errors are thus judged small or large relative to the magnitude of σ^2 (Schmittner et al., 2009). Following Steinacher et al. (2013) and Schmittner et al. (2009), we estimate σ^2 as the volume-weighted variance of the model-data residuals for the ensemble member with the lowest MSE such that the best fitting ensemble member has a MSE^{rel} close to unity. The different MSE^{rel} (here three) are averaged to a total $\text{MSE}_{\text{tot}}^{\text{rel}}$ to yield a skill score S_m as follows:

$$S_m = \exp(-0.5 \cdot \text{MSE}_{\text{tot}}^{\text{rel}}). \quad (7)$$

S_m is a likelihood-type function and corresponds to a Gaussian distribution of the data-model residuals with zero mean and variance σ^2 . S_m can be interpreted as an indication of the relative performance of each individual model configuration, where configurations which have relatively small deviations from the data are considered more probable than configurations which differ more from the observations. S_m are used as weight to compute probability density functions (PDFs) and related measures such as the median (50th percentile) and 68% confidence interval ($\pm 1\sigma$, the 16th to 84th percentile range) of the ensemble results. The methodology follows earlier papers of Steinacher et al. (2013), Steinacher and Joos (2016), and Battaglia et al. (2016).

Three observational data sets (Table 2) are used to constrain marine N_2O emissions. We use (1) water column $[\text{N}_2\text{O}]$ data and (2) surface pN_2O measurements from the MEMENTO database (Kock & Bange, 2015, accessed 23.11.2016). The measurements are assigned to the corresponding Bern3D grid cell. Different measurements on the same grid cell are averaged using distance weighting. Another score based only on the (3) mean N_2O concentrations below 1.5 km in each basin (three values for each run) is calculated in addition. This is to ensure that $[\text{N}_2\text{O}]$ in the deep ocean is not overestimated.

Table 2
Observational Data Used to Constrain the Model Ensemble

Variable	Reference	Time frame of model
(1) Dissolved N ₂ O (~10% of all grid cells)	MENTO, Kock and Bange (2015)	1990–2005
(2) Surface pN ₂ O (~50% of surface grid cells)	MENTO, Kock and Bange (2015)	1977–1995
(3) N ₂ O mean concentration below 1,500 m in each basin (three average values from 426 (Atlantic), 138 (Pacific), and 62 (Indian) measurements on the Bern3D grid)	MENTO, Kock and Bange (2015)	1990–2005

We average the modeled N₂O over the time period 1990–2005 (a 15 year period until the start of the RCP scenarios) and the modeled pN₂O over 1977–1995 where most observations were made. The N₂O skill scores are insensitive to the time periods considered for averaging.

σ^2 is estimated based on the variance of the model-data residuals for the ensemble member with the lowest MSE as described above. The only exception is constraint (3). Here σ^2 is taken as the variance of all observations below 1.5 km. In a final evaluation step we penalize members which have a correlation coefficient of less than 0.35 (score 0 by choice). See sections 3 and 4 for a discussion.

Sensitivity tests with smaller ensembles were used to determine plausible prior ranges for the parameters describing nitrification and denitrification. In addition, the parameters affecting mixing ($k_{diff-dia}$) and aerobic organic matter remineralization (α_{aerob}) have been tuned during the development of Bern3D with respect to O₂, natural $\Delta^{14}C$, and CFC distributions (Battaglia et al., 2016; Gerber & Joos, 2013; Roth, 2013). Here these two parameters are sampled within relatively narrow ranges such that all members achieve similar and good skill scores with respect to O₂ and natural $\Delta^{14}C$ distributions. This represents a preselection step in the model evaluation and acknowledges uncertainties in circulation and remineralization fluxes. The remineralization coefficients (α_{aerob} and α_{denit}) and the O₂ thresholds (μ and σ) tend to have compensatory effects on modeled O₂ and remineralization fluxes (see also similar case in supporting information of DeVries et al., 2013). Only the remineralization parameters are therefore sampled in the Monte Carlo framework in order to minimize the degrees of freedom and facilitate interpretation. The scaling factor in the Martin curve is 1 order of magnitude lower for remineralization by denitrification (α_{denit}) than for aerobic remineralization (α_{aerob}). This low range of values for (α_{denit}) is consistent with the available observational evidence and reproduces remineralization fluxes in line with estimates of total N loss as summarized by Yang and Gruber (2016).

2.4. Experimental Design

Each model run is first spun-up over 5,000 years to a preindustrial steady state, with atmospheric CO₂ set to 278 ppm and N₂O to 272.96 ppb. Over the industrial period (A.D. 1765–2005) we include CO₂ and non-CO₂ radiative forcings according to Eby et al. (2013) and we prescribe the atmospheric N₂O history according to Meinshausen et al. (2011). From A.D. 2005 to A.D. 3000 the RCP2.6 and RCP8.5 scenarios (Meinshausen et al., 2011) are prescribed similar to the constant composition commitment simulations in Zickfeld et al. (2013). Simulations are extended from year A.D. 3000 to year A.D. 10,000 for the 200 members with the highest skill score. After year A.D. 3000, the concentrations and radiative forcings are kept constant (Figure 9a). The cumulative weight of the 200 best simulations is 54% of the total weight. These 200 members yield a $\pm 1\sigma$ range of 2.6 to 5.0 Tg N yr⁻¹ for modern N₂O production. This is lower than for the full ensemble (3.0 to 6.1 Tg N yr⁻¹) (see Figure D1 for an illustration of the skill score).

The equilibrium climate sensitivities (ECSs) of the model configurations range between ~3.5 and ~4°C for a doubling of atmospheric CO₂. The range reflects variations in the diapycnal mixing coefficient ($k_{diff-dia}$). These ECSs are at the higher end of values summarized in the latest report of the Intergovernmental Panel on Climate Change (IPCC) (likely between 1.5 and 4.5°C; T. Stocker et al., 2013). The current model configuration does not include sediment interactions, temperature-dependent remineralization, variable stoichiometry, nitrogen cycle feedbacks, atmospheric nutrient deposition, dynamic wind, nor freshwater input/albedo changes from melting of continental ice sheets.

We distinguish marine N₂O production from each individual production term. N₂O production from nitrification results from two components: (i) the constant nitrification yield (“ α term” in equation (1) and (ii) the

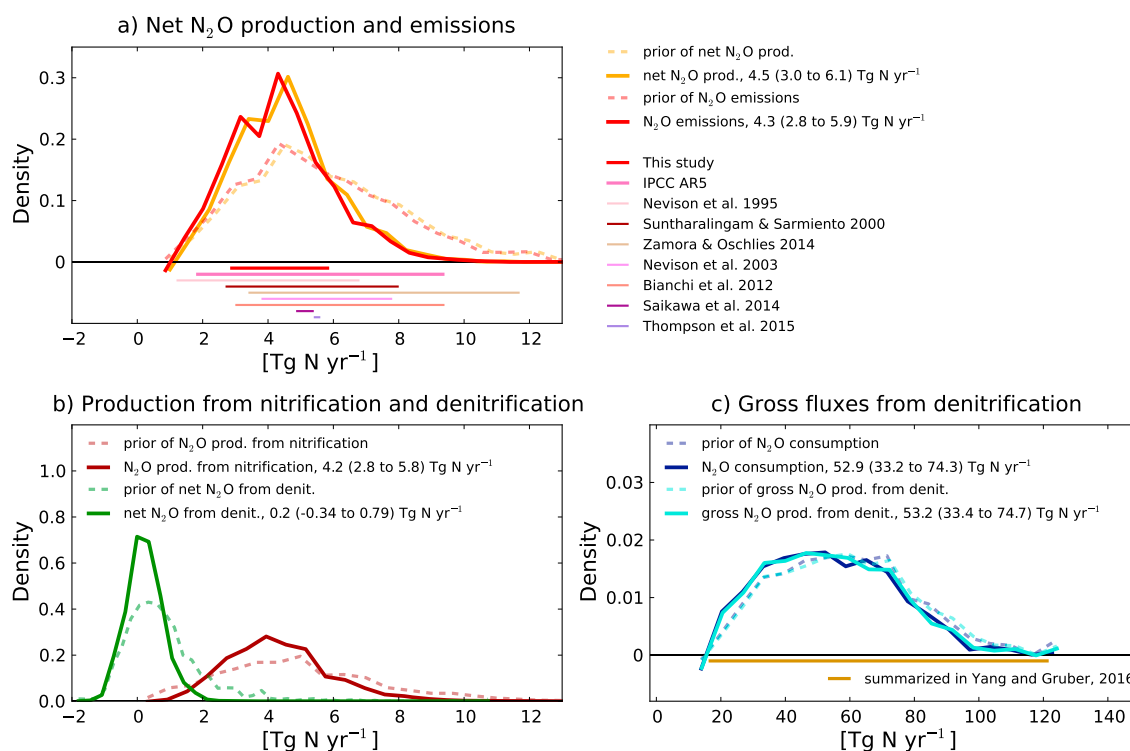


Figure 2. Probability density functions (PDFs) of modeled N_2O fluxes. (a) Net N_2O production and air-sea exchange, (b) net oceanic N_2O production from nitrification and denitrification, and (c) gross production and consumption by denitrification. Dashed curves indicate the associated prior and continuous curves the constrained posterior PDFs. Straight lines below the PDFs indicate associated ranges published in the literature. In Figure 2a estimates from Ciais et al. (2013), Nevison et al. (1995), Suntharalingam and Sarmiento (2000), Zamora and Oschlies (2014), Nevison (2003), Bianchi et al. (2012), Saikawa et al. (2014), and Thompson et al. (2014). In Figure 2c estimates of total N loss as summarized by Yang and Gruber (2016) converted to N loss by conversion to N_2 from denitrification given the here assumed stoichiometric ratios (see main text).

O_2 -dependent nitrification yield (" $\beta \cdot f(\text{O}_2)$ " term" in equation (1), $[\text{N}_2\text{O}_\beta]$). (iii) "Net denitrification" results from (iv) N_2O production minus (v) N_2O consumption by denitrification (equations (4) and (5)). N_2O from both nitrification terms, from net denitrification and N_2O 's solubility component, are explicitly carried as model tracers. Tracers add up to within $10^{-11} \mu\text{mol m}^{-3}$. This way, the model-data differences can be attributed to processes. The oceanic N_2O inventories are separated in a biological production component (including all production terms) and a solubility component. Changes in emissions due to changes in storage can therefore be disentangled. Additional tracers (O_2 solubility component, remineralized nutrients, ideal age) are included to aid the interpretation of the future projections.

3. Results

3.1. Current N_2O Production From Nitrification and Denitrification

The constrained model ensemble yields an average global median (and $\pm 1\sigma$ range) net N_2O production of 4.5 (3.0 to 6.1) Tg N yr^{-1} for the time period 1990 to 2005 (Figure 2a). Noticeably, the observational constraints shift the prior distribution of N_2O production to lower values (Figure 2, dashed versus solid lines). The sampled (prior) N_2O production ranges from 1.0 to over 13 Tg N yr^{-1} (Figure 2a). The 1990 to 2005 average global mean sea-to-air flux is slightly lower than N_2O production, 4.3 (2.8 to 5.9) Tg N yr^{-1} , as rising atmospheric N_2O leads to a solubility driven oceanic N_2O uptake anomaly. The observation-constrained range of global emissions is narrower than the range of 1.8 to 9.4 Tg N yr^{-1} summarized in the IPCC AR5 (see pink line in Figure 2a), IPCC AR5 Ciais et al., 2013).

About 96.0% of net production stems from nitrification, 4.2 (2.8 to 5.8) Tg N yr^{-1} , with the reminder from denitrification, 0.2 (-0.34 to 0.79) Tg N yr^{-1} (Figure 2b). The small net contribution from denitrification results from large gross N_2O fluxes (Figure 2c). About 52.9 (33.2 to 74.3) Tg N yr^{-1} are consumed and 53.2 (33.4 to 74.7) Tg N yr^{-1} produced (median values of gross fluxes do not add up to the median net flux of 0.2 Tg N yr^{-1}).

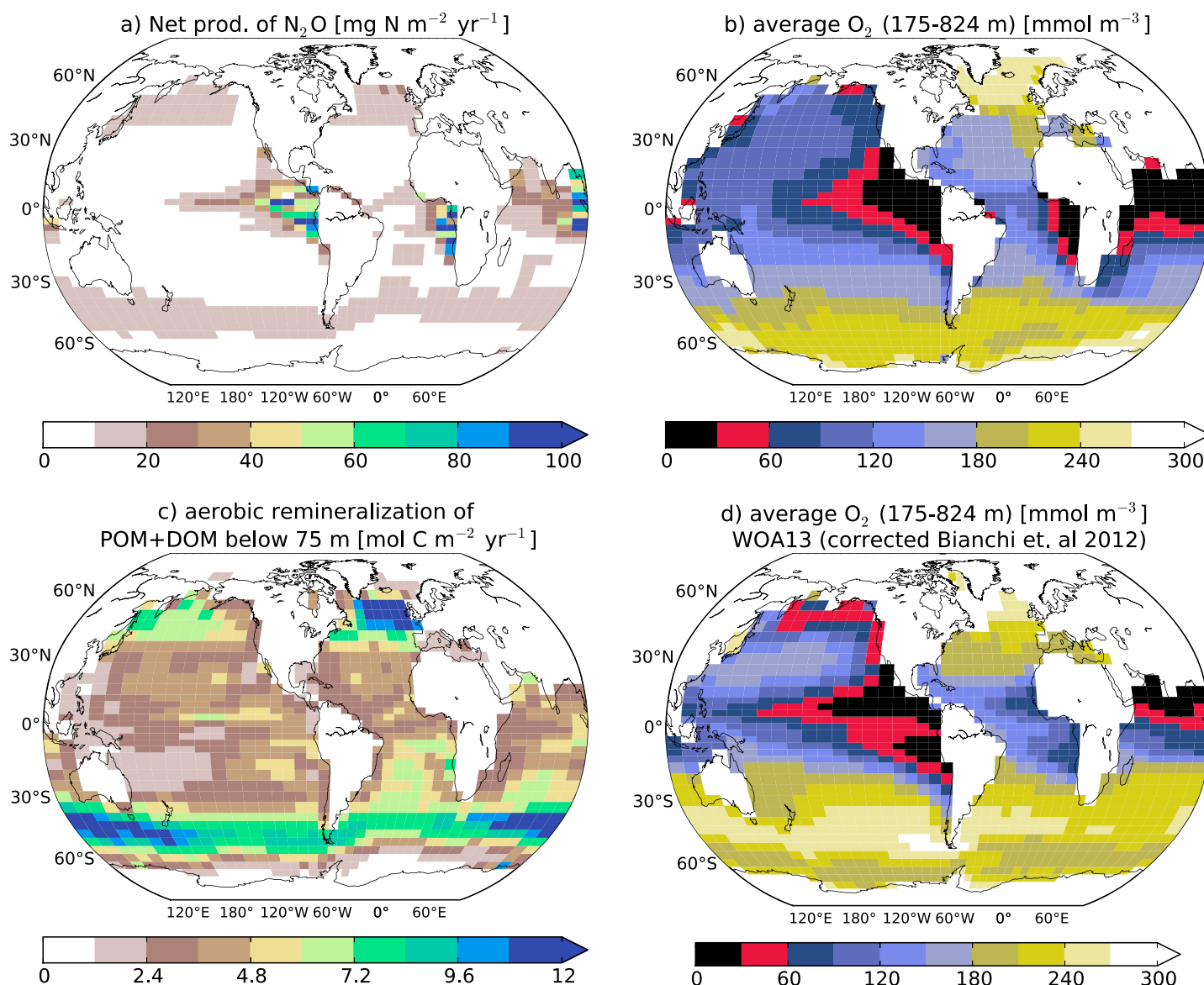


Figure 3. Maps of variables of interest. Modeled median (a) net production of N_2O , (b) average $[\text{O}_2]$ in the upper ocean (175–824 m depth), and (c) aerobic remineralization of POM and DOM below 75 m for the time period 1990 to 2005. (d) The average upper ocean $[\text{O}_2]$ of WOA13 (Garcia et al., 2014; Bianchi et al., 2012).

The N_2O consumption flux of $52.9 \text{ Tg N yr}^{-1}$ represents the conversion of N_2O to N_2 (equation (C2)). In addition, NH_3 produced during N_2O production and consumption (equations (C1) and (C2)) is likely also oxidized to N_2 ($\text{NH}_3 + 3/5 \text{ HNO}_3^- \rightarrow 4/5 \text{ N}_2 + 9/5 \text{ H}_2\text{O}$; equation 17 in Paulmier et al., 2009). Total N loss by conversion to N_2 amounts then to 65.1 (40.9 to 91.6) Tg N yr^{-1} , given the assumed stoichiometric ratios. This compares very well with estimates of total N loss from denitrification which span 20 – 150 Tg N yr^{-1} as summarized by Yang and Gruber (2016). Modeled global export of particulate organic carbon out of the euphotic zone is 9.88 (9.19 to 10.6) Gt C yr^{-1} . This estimate from the constrained model ensemble is well within published estimates (Sarmiento and Gruber, 2006, 6.5 to $13.1 \text{ Gt C yr}^{-1}$) but higher than what CMIP5 models simulate (4.9 to 8.1 Gt C yr^{-1} , Bopp et al., 2013). Aerobic remineralization of dissolved and particulate organic carbon below the euphotic zone is 19.7 (18.2 to 21.2) Gt C yr^{-1} , and anaerobic remineralization below the euphotic zone is 48.3 (30.3 to 67.7) $10^{-3} \text{ Gt C yr}^{-1}$.

The geographic pattern of water column-integrated N_2O production (Figure 3a) resembles to some extent that of POM export and water column-integrated aerobic remineralization (Figure 3c). High N_2O production

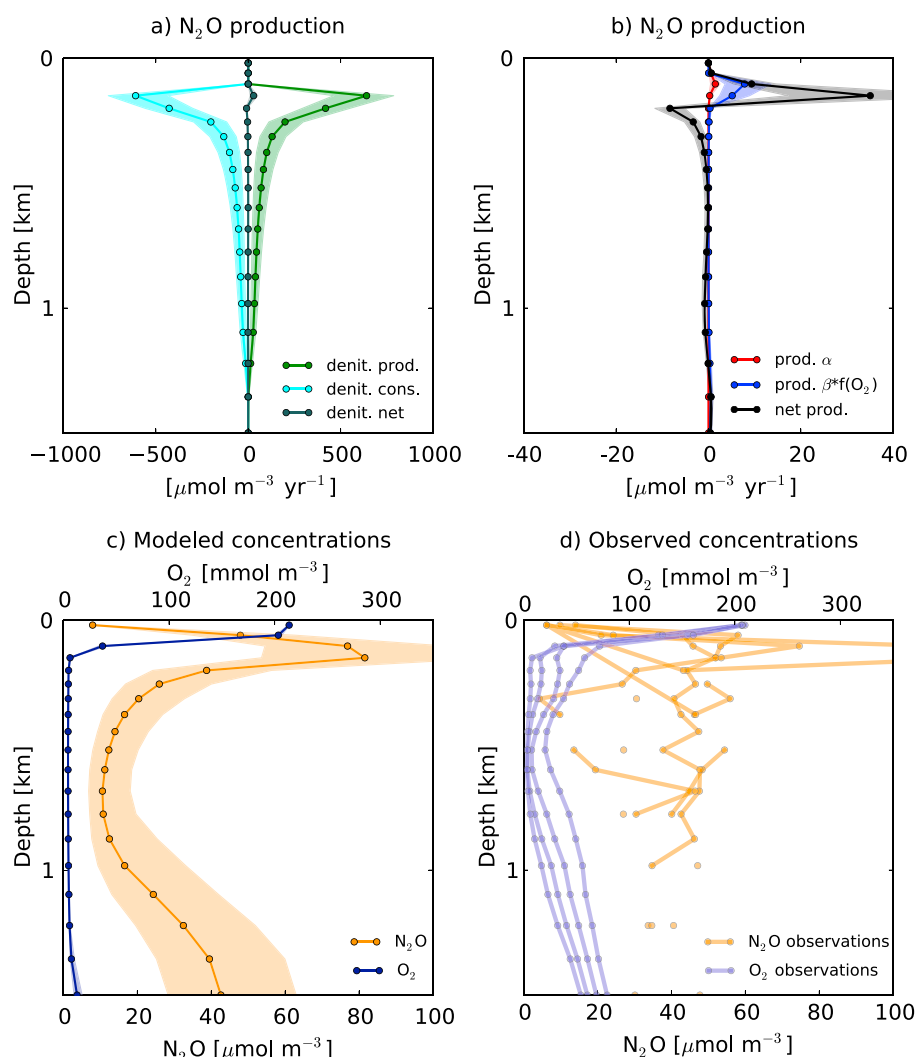


Figure 4. Profiles at 10.5°N and 98°W. (a) Modeled N_2O production and consumption from denitrification. (b) Net N_2O production and N_2O production from the two nitrification terms. (c) Modeled N_2O and O_2 concentrations. Lines correspond to modeled median and ranges to the 68% confidence interval given by the ensemble. (d) Observational profiles of N_2O and O_2 at four neighboring locations. Production from α refers to the constant nitrification yield, and production from $\beta^*f(O_2)$ refers to the O_2 -dependent nitrification yield.

is simulated in the high biological productivity regions of the Southern Ocean, the northern North Pacific, and North Atlantic, and low N_2O production is simulated in the oligotrophic gyre regions. In these regions, N_2O production scales approximately linearly with aerobic remineralization. Simulated $[O_2]$ are high (Figure 3b) such that the N_2O yield is approximately constant (close to constant nitrification yield, α , equation (1)). N_2O production is highest in the low-oxygen regions of the eastern tropical Pacific, Atlantic, and Indian Oceans. Here moderate-to-high remineralization combines with highest N_2O yields (equation (1)) for nitrification. In addition, N_2O is affected by denitrification. The interplay of the different fluxes within low oxygen waters is illustrated at a profile located in the Pacific Oxygen Minimum Zone (OMZ) at 10.5°N and 98°W. Here modeled O_2 concentrations decrease rapidly from the surface and allow for denitrifying conditions over the first kilometer. The modeled N_2O profile exhibits a typical structure (Figure 4c) with a N_2O peak at shallow depths, a broad minimum at intermediate depths in the thermocline and increasing $[N_2O]$ toward the deep ocean. Gross fluxes from denitrification are ~ 50 times higher than those from nitrification (Figure 4a), and nitrification and denitrification can co-occur within grid cells (Figure 4b). The modeled consumption rates are comparable to the N_2O consumption rates measured at offshore stations by Babbitt et al. (2015, $\sim 2 \text{ nmol L}^{-1} \text{ d}^{-1} = 730 \mu\text{mol m}^{-3} \text{ yr}^{-1}$). Observational profiles of N_2O at neighboring locations show high variability (Figure 4d). This small-scale variability makes it difficult to match individual N_2O observations in the simulations.

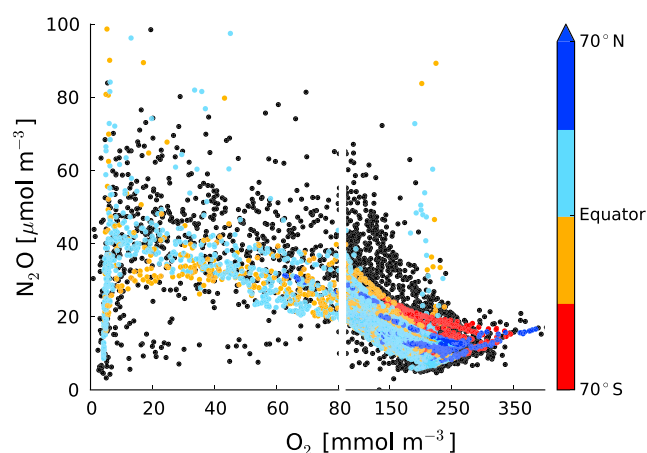


Figure 5. Modeled median (colors) and observed (black) relationship between N_2O and O_2 concentrations. The colors indicate the latitudinal position of each modeled N_2O - O_2 pair ranging from 70°S to 72.5°N .

3.2. Evaluation of Modeled N_2O and O_2 Concentrations

We start the model-data comparison with the relationship between N_2O and O_2 concentrations (Figure 5) before turning to the actual N_2O and O_2 distributions, separately. Median fields are chosen for evaluation purposes. We note that median fields are, by definition, not necessarily physically self-consistent. However, individual runs with N_2O production close to the median fluxes and a run with the best guess parameters provided in Table 1 produce fields for individual N_2O production terms, N_2O emissions, and for N_2O concentrations that show generally small differences compared to the corresponding median fields.

The N_2O and O_2 relationship is important given the critical role of O_2 concentrations in setting both the N_2O yield from nitrification and in separating aerobic remineralization from denitrification. Generally, the observed relationship is matched by the model (colored versus black dots in Figure 5). Three features stand out. First, the model reproduces the widespread of $[\text{N}_2\text{O}]$ observed at very low $[\text{O}_2]$ (N_2O spanning $5\text{--}100\text{ }\mu\text{mol m}^{-3}$). Such conditions prevail in equatorial regions (see colors in Figure 5 indicating the latitudinal position). Consumption and produc-

tion by denitrification is critical to achieve this spread. Second, modeled N_2O at O_2 concentrations spanning $20\text{--}150\text{ mmol O}_2\text{ m}^{-3}$ is well within the observational range, while modeled variability of N_2O is lower than observed (black dots in Figure 5). Most of the observations at these intermediate O_2 have been made in equatorial regions, too. Third, at high $[\text{O}_2]$ ($>200\text{ mmol O}_2\text{ m}^{-3}$), where essentially background $[\text{N}_2\text{O}]$ prevail, model-data agreement is good. Such conditions prevail in high-latitude waters.

We now examine modeled $[\text{N}_2\text{O}]$ in more detail. The MEMENTO database of marine N_2O measurements (Kock & Bange, 2015) currently covers $\sim 10\%$ of the ocean volume. This low coverage, combined with the small-scale variability of N_2O , hampers any model-data comparison. Globally, the modeled RMSE is $11.1\text{ }\mu\text{mol N}_2\text{O m}^{-3}$ with a correlation coefficient r of 0.52 between simulated median and observed $[\text{N}_2\text{O}]$. Other modeling studies achieve similarly low correlation coefficients (Martinez-Rey et al., 2015, their P. OMZ parameterization: $r = 0.42$, their P. TEMP parameterization: $r = 0.49$) but usually have higher errors (see Figure 3 of Martinez-Rey et al., 2015). In Figure 6, we compare measured and simulated N_2O profiles for three latitudinal bands in the Atlantic, Pacific, and Indian. In the northern North Atlantic, measured and simulated $[\text{N}_2\text{O}]$ are close or somewhat above the saturation concentration relative to atmospheric N_2O ($10\text{ }\mu\text{mol m}^{-3}$) and model-data agreement is high, except below 3.5 km, where the model tends to overestimate $[\text{N}_2\text{O}]$. Reasonable to good data-model agreement is also found in the Southern Ocean where N_2O increases from saturation concentration at the surface to about $20\text{ }\mu\text{mol m}^{-3}$ in the upper 1,000 m below which it remains relatively constant. In the North Pacific, the model median underestimates peak concentrations found at $\sim 1\text{ km}$ depth. In equatorial regions, observed $[\text{N}_2\text{O}]$ are highly variable ($\sigma = 14.7\text{ }\mu\text{mol m}^{-3}$) and reach concentrations up to $126.4\text{ }\mu\text{mol m}^{-3}$ within the upper ocean. In the lower water column of equatorial regions, measured concentrations show smoother profiles back to more uniform values of $15\text{--}20\text{ }\mu\text{mol m}^{-3}$. The model fails to produce the observed high (small-scale) variability in the upper ocean of equatorial regions, particularly so in the Pacific. Modeled profiles generally are smoother than observed (compare also Figures 4c and 4d). In equatorial regions, high net positive N_2O production from denitrification close to the surface can lead to single high outliers in the model (up to $203\text{ }\mu\text{mol m}^{-3}$) which are not present in the Bern3D gridded MEMENTO database. Nevertheless, high $[\text{N}_2\text{O}]$ have been reported, $\sim 250\text{ }\mu\text{mol m}^{-3}$ (Arévalo-Martínez et al., 2015), $986\text{ }\mu\text{mol m}^{-3}$ (Arévalo-Martínez et al., 2016), $533\text{ }\mu\text{mol m}^{-3}$ (Naqvi et al., 2000), and $\sim 850\text{ }\mu\text{mol m}^{-3}$ (Kock et al., 2016). Consumption of N_2O by denitrification is critical to reduce concentrations in these hot spot environments to essentially solubility concentrations. The model thereby simulates steep concentration gradients in these regions but on larger spatial scales than observed. Data-model misfits exist in bottom waters along the coast of the eastern equatorial Pacific. Ocean-sediment interactions are not included in the model setup, and all organic matter reaching the seafloor is nitrified in the model. Below low O_2 waters, a larger fraction of exported organic matter reaches the seafloor in comparison with a fully aerobic water column (see also Figure 1a). This apparently leads to an overestimation of local N_2O production. Near-seafloor production is relatively small and amounts to $\sim 5\%$ of net N_2O production in the Pacific.

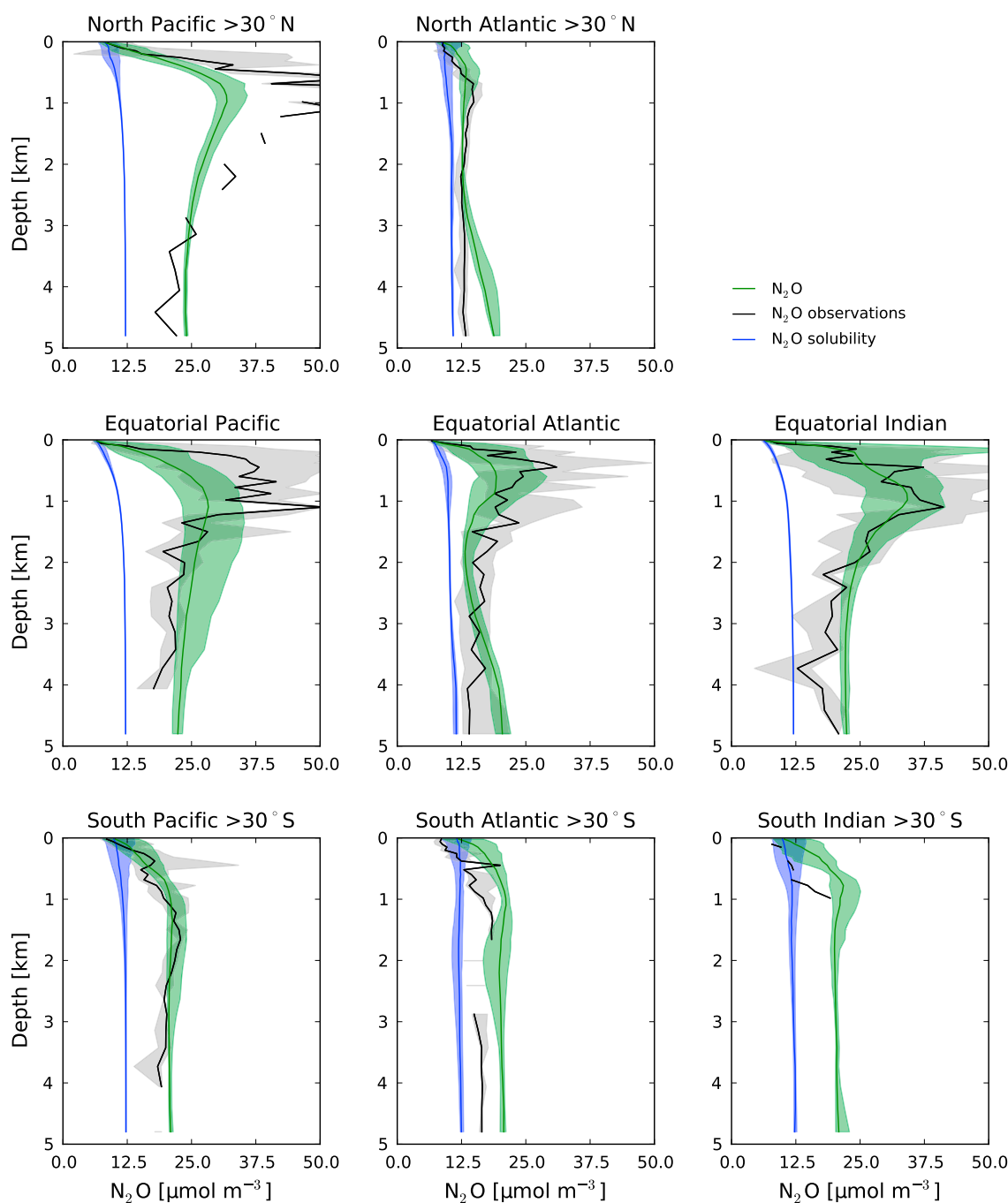


Figure 6. Spatial spread of modeled median and observed $[N_2O]$ within different geographic regions (see title of subplots). The green line represents the median concentration, and the green (gray) shadings represent the spatial spread (16th to 84th percentile of the median (observational) field). Blue: modeled solubility component, green: modeled N_2O , and black: observations.

In the following, we turn to the modeled distribution of O_2 . The Bern3D model does simulate low O_2 environments in eastern boundary upwelling systems of all basins (compare Figures 3b and 3d). In the Equatorial Pacific, the EMIC fails to resolve Equatorial Undercurrents. The OMZ here is therefore one coherent region rather than showing two distinct regions separated by a well-ventilated band. In the North Pacific, modeled $[O_2]$ are too high; in the equatorial Atlantic, modeled $[O_2]$ are too low; and in the Indian Ocean, the volume of low O_2 waters is too large (Figures 3b and 3d). Despite these shortcomings, a frequency diagram reveals similar frequency distributions for modeled and observed oxygen (Figure 7a). Both model and observation-based distributions cover a range between 0 and 400 $mmol\ O_2\ m^{-3}$ and show two peaks around

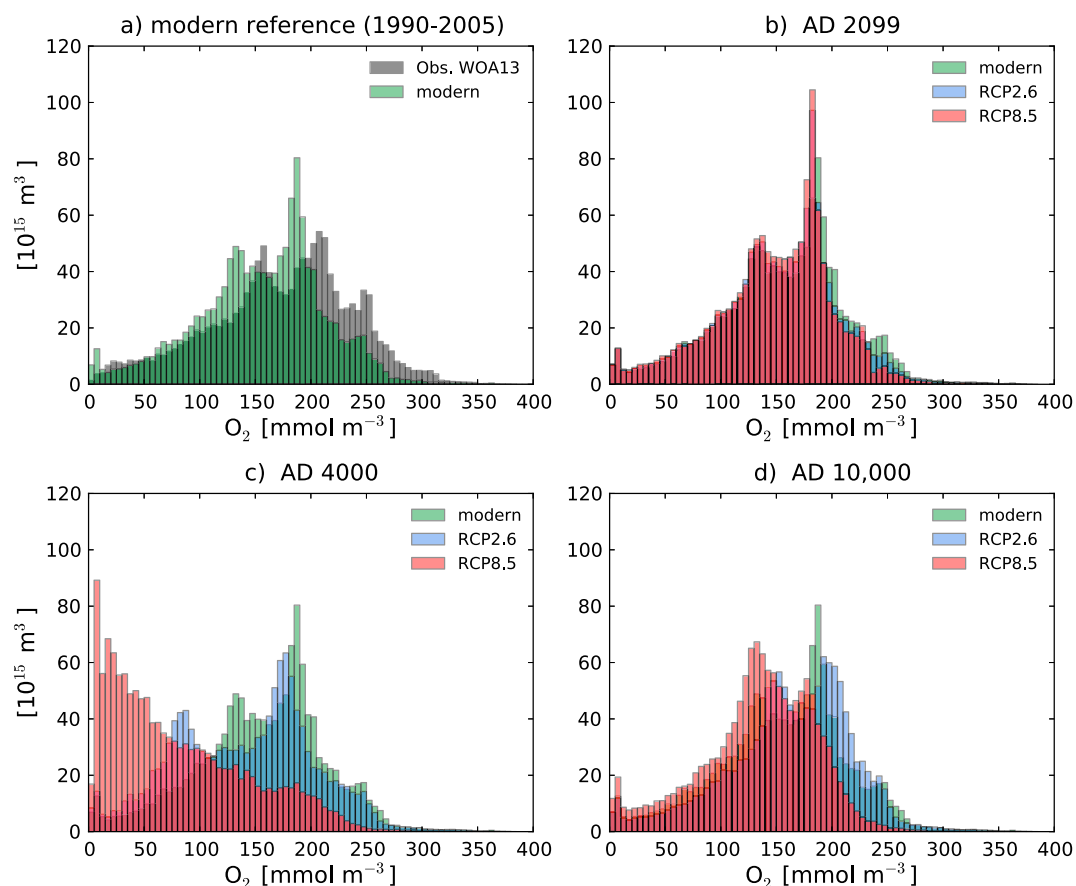


Figure 7. Volume-weighted histograms of modeled median and observed $[O_2]$. (a) Evaluation of median $[O_2]$ for the modeled modern reference period (1990–2005) with WOA13 (Garcia et al., 2014; Bianchi et al., 2012) and (b) projections of modeled median $[O_2]$ at model year A.D. 2099, (c) at model year A.D. 4000 and (d) at model year A.D. 10,000. The modeled reference period is included in Figures 7b–7d for comparison.

150 and 200 mmol O_2 m^{-3} . Importantly, the median model results feature a realistic extent of low O_2 environments. The modeled volume of water with $[O_2] < 80$ mmol m^{-3} and with $[O_2] < 50$ mmol m^{-3} matches observation-based estimates within some percent (see Table D1). As most models, the Bern3D model overestimates the volume of water with $O_2 < 5$ mmol O_2 m^{-3} by about a factor of 5. This is less than found for the Earth System models considered in Cocco et al. (2013), except for the IPSL model which underestimates the volume occupied by suboxic waters (Table D1).

3.3. The Role of Individual Observational Constraints

In this section we address how the observational constraints (Table 2) used in the skill assessment constrain the parameter ranges and resulting N_2O fluxes. Recall that skill scores are set to zero if the correlation between observed and modeled $[N_2O]$ is less than 0.35. This serves as an additional constraint. As mentioned in section 2.3, the parameters were sampled within plausible ranges as informed by literature values and preceding simulations with a smaller ensemble size. The constrained ensemble shows substantially narrower distributions for N_2O production and air-sea fluxes than present in the unconstrained ensemble. This finding lends support to our approach.

The observational constraints reject both very low and very high net N_2O production and sea-to-air fluxes. The confidence intervals obtained when only including one constraint in the skill computation are similar (Figure 8). The surface partial pressure data constraint yields lower production than inferred from the water column concentration constraints. The combination of all constraints yields the narrowest confidence interval (3.1 versus 3.7 Tg N yr^{-1}). In a further sensitivity test, we added observation-based O_2 and natural $\Delta^{14}C$ as two additional constraints. This yields slightly higher median values and ranges than the standard computation

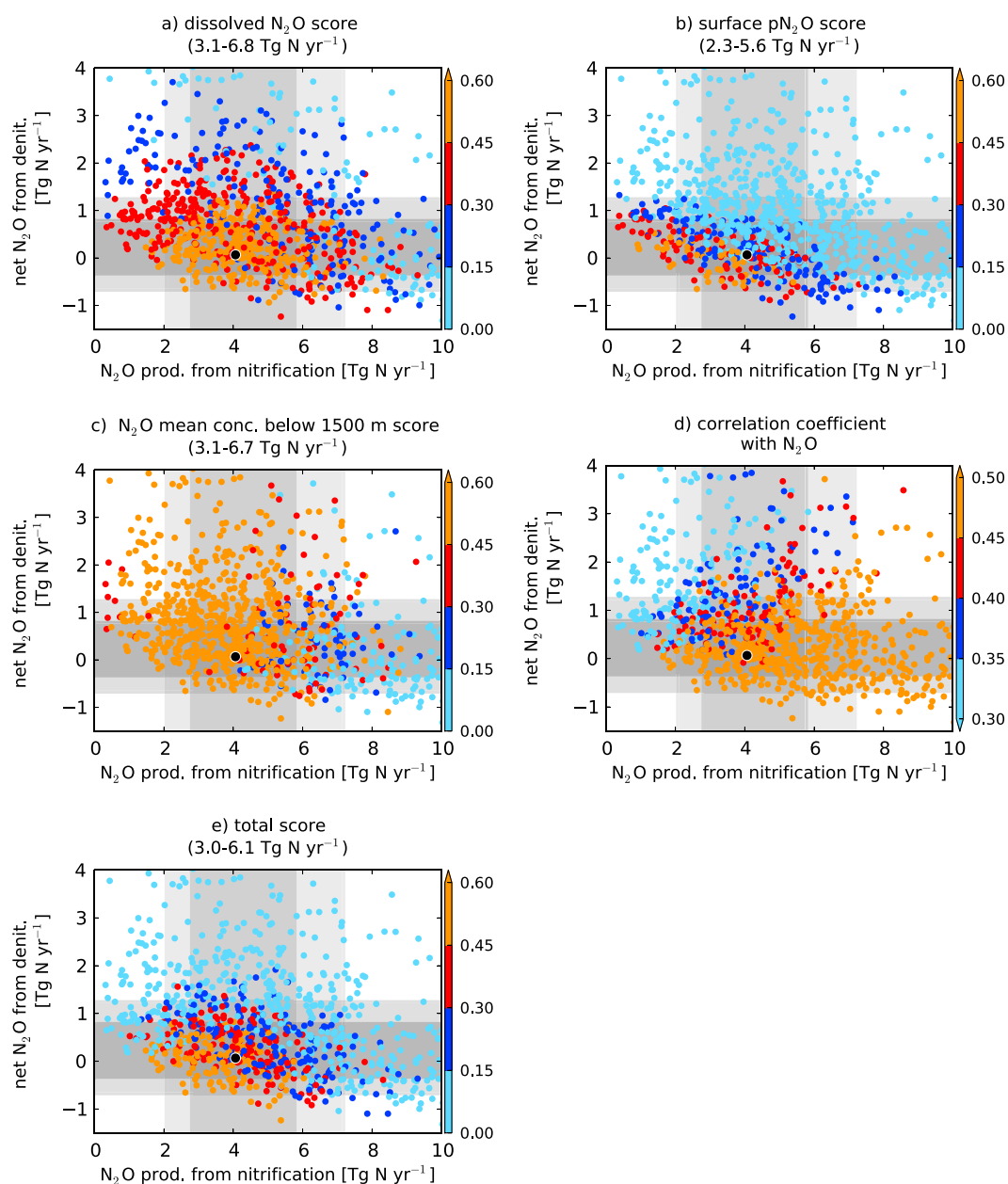


Figure 8. Impact of different observational constraints on N_2O production from nitrification (x axis) and net N_2O production from denitrification (y axis). Colors represent scores for the individual observational targets described in Table 2, namely, (a) dissolved N_2O , (b) surface pN_2O , (c) mean N_2O concentration below 1,500 m, and (d) the correlation coefficient and (e) the total score. Values given in parenthesis represent the net N_2O production if only the respective score is considered. Gray shading marks the 90% and 68% confidence interval for the respective fluxes using the total score. The black dot represents the selected best consistent model with parameters given in Table 1.

(4.7 (3.2 to 6.6) Tg N yr^{-1}). In brief, our results are moderately sensitive to choices such as whether an individual constraint is included or not and how exactly the individual constraints are aggregated in the skill assessment.

Low net N_2O production from nitrification ($<2 \text{ Tg N yr}^{-1}$) yields on average low absolute errors, but correlation between modeled and measured N_2O fields is also very low (Figure 8d). Members with low productivity are therefore rejected as we require correlation coefficients to be larger than 0.35 (section 2.3). Very high production by nitrification, on the other hand, leads to too high background concentrations in the deep ocean via transport and mixing and to low skill (Figure 8c). The additional skill score computed from deep basin-averaged N_2O concentrations (data set (3) in Table 2) therefore constrains nitrification at the high end.

The surface pN_2O data alone hardly constrain N_2O production from nitrification (Figure 8b). The N_2O production related to the constant yield factor for nitrification (α term in equation (1)) is hardest to constrain. These fluxes yield a smooth background $[N_2O]$ field in the entire ocean which does not lead to pronounced errors. Ensemble members with net N_2O production by denitrification higher than $\sim 2 \text{ Tg N yr}^{-1}$ yield results in conflict with water column N_2O data, and those with net N_2O production by denitrification higher than $\sim 1 \text{ Tg N yr}^{-1}$ yield results in conflict with surface pN_2O (Figures 8a and 8b). These ensemble members have low skill scores.

A single run is highlighted in Figure 8 (black dot). This run reproduces the median fluxes presented and can be regarded as a best consistent model. Evaluation of its N_2O and O_2 fields is comparable to the median fields presented in section 3.2, and its parameter values are included in Table 1. This best consistent model configuration may be chosen for paleomodeling studies.

3.4. Future Projections

The short- and long-term responses of marine N_2O production and marine N_2O emissions to increased levels of GHGs are different. N_2O production and emissions are projected to first decrease over the 21st century (7.7% less net production compared to the modern reference period). Thereafter, N_2O production and emissions are projected to increase to reach higher levels under new steady state conditions (21% higher net production compared to the modern reference period). The changes result from changes in meridional overturning, deoxygenation, warming, and resulting changes in remineralization fluxes. We look at each of these contributing factors in turn to explain the N_2O signal in more detail (Figure 9 and Table D2). In Table D2, the modern reference median values and $\pm 1\sigma$ ranges of the variables of interest are given along with the changes by the end of the 21st century and the changes for new steady state conditions by A.D. 10,000 for both the RCP2.6 and RCP8.5 GHG scenario. Changes are expressed relative to the modern reference period. We focus the following discussion on the RCP8.5 scenario.

3.4.1. Transient Circulation Changes, Export Production, and Deoxygenation

In response to the constant composition commitment scenario RCP8.5, atmospheric temperatures rise and stabilize after $\sim 1,000$ years. For the ocean, it takes $\sim 4,000$ years to reach a new thermal equilibrium (Figure 9c, 7.2°C warmer compared to today). As temperatures rise and surface density decreases, meridional overturning in the ocean slows down (Figure 9e) in line with other global warming modeling studies (T. Stocker et al., 2013). Here meridional overturning in the Atlantic (AMOC) decreases by 42% at A.D. 2100 compared to the modern reference period and recovers to preindustrial levels thereafter. In the new steady state conditions, the upper cell of the AMOC becomes shallower in the Bern3D. An AMOC slowdown and partial or full recovery emerges in other multimillennial simulations (Li et al., 2013; Schmittner et al., 2008; Weaver et al., 2012; Zickfeld et al., 2013). No recovery of the AMOC was found in Yamamoto et al. (2015 $4\times\text{CO}_2$ simulation). In our simulations, the peak weakening of meridional overturning in the Indo-Pacific follows after the one in the North Atlantic (-52% compared to the modern reference period), and its recovery is slower. After $\sim 3,000$ years of simulation, the Indo-Pacific MOC overshoots preindustrial conditions in the Bern3D and stabilizes thereafter at a higher level ($+27\%$ compared to the modern reference period). The mechanisms involve increased precipitation, reduced sea ice formation, and weaker vertical mixing which lead to a strong initial freshening and stratification in surface deep water formation regions in the Southern Ocean. After $\sim \text{A.D. } 2100$, sea ice formation is absent. At higher overall temperatures and in the absence of sea ice formation stronger deepwater formation results for the new steady state. Ocean ventilation is also affected by convection (not analyzed within the scope of this work). A reduction and a slow increase toward recovery of the Indo-Pacific MOC have also been reported by Schmittner et al. (2008, SRES A2 scenario) over a 2000 year simulation involving similar mechanisms. In Yamamoto et al. (2015 $4\times\text{CO}_2$ simulation), Antarctic Bottom Water formation initially decreases and overshoots preindustrial levels after 1,000 years. In their model simulation, enhanced deep ocean convection contributed to enhanced ventilation. Generally, pre-industrial circulation states, magnitudes, and timing of changes highly depend on model configurations and applied forcings such that the long-term evolution of meridional overturning remains uncertain. Most global warming simulations, including ours, do not include melting of continental ice sheets, which would tend to further (transiently) reduce circulation (Bakker et al., 2016).

The transient slow down of ocean ventilation impacts tracer distributions and export production. Deep ocean water masses age, remineralized nutrients accumulate, $[O_2]$ decreases, and it takes millennia to re-equilibrate

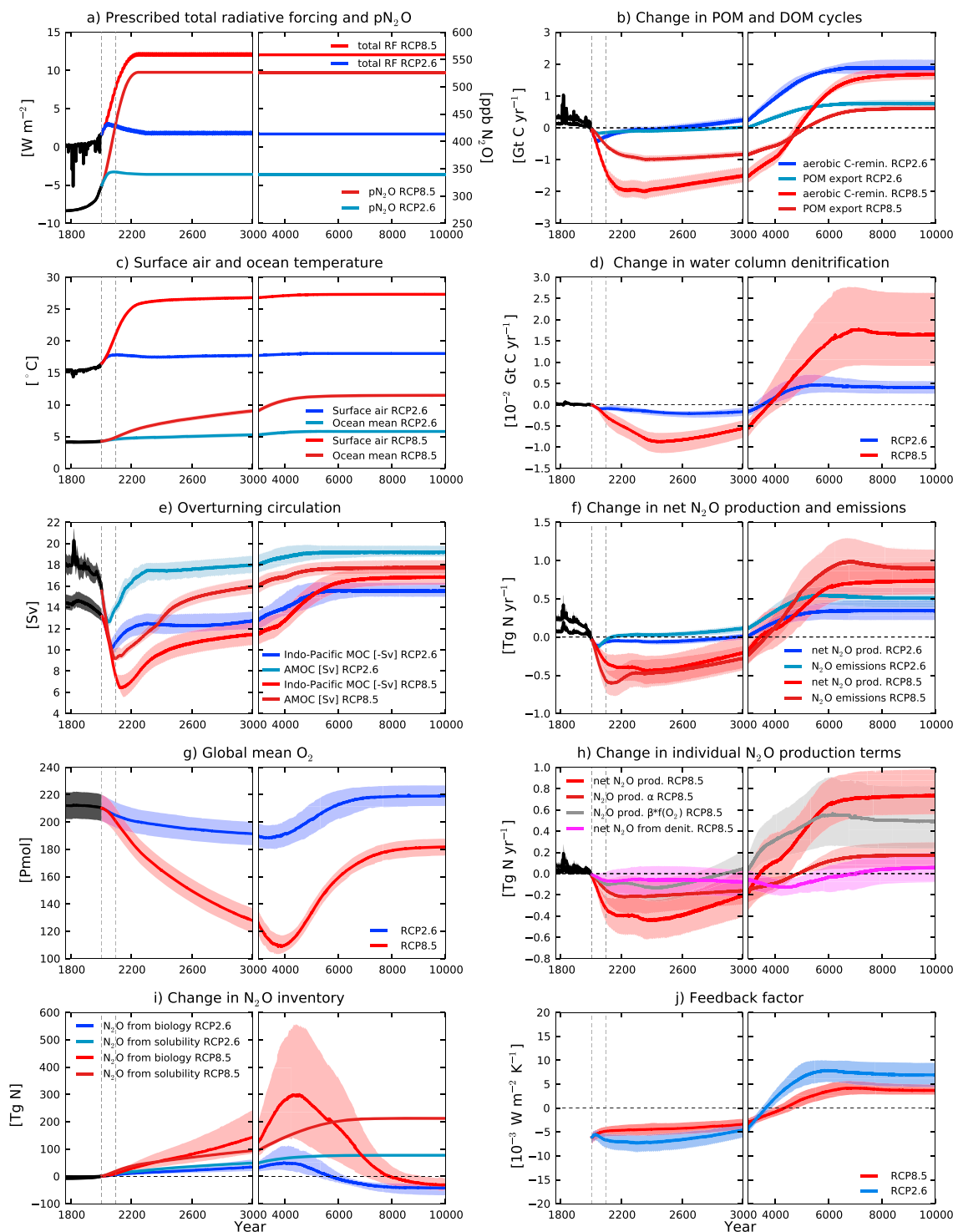


Figure 9. Time series of physical and biogeochemical variables as simulated over the industrial period and projected for RCP2.6 (blue) and RCP8.5 (red). A reduced ensemble, including only the 200 members with the highest skill (S_m), is used after A.D. 3000. See Table D2 for modern reference values and changes at A.D. 2099 and A.D. 10,000. (e) Indo-Pacific MOC is the minimum of the Indo-Pacific and AMOC is the maximum of the Atlantic meridional overturning stream function below 400 m depth. (h) The changes in individual N₂O production terms are shown only for RCP8.5. Production from α refers to the constant nitrification yield, and production from $\beta \cdot f(\text{O}_2)$ refers to the O₂-dependent nitrification yield. (j) The climate feedback factor for changing marine N₂O emissions is expressed relative to preindustrial (see section 3.5; values are shown from 2000 A.D. onward).

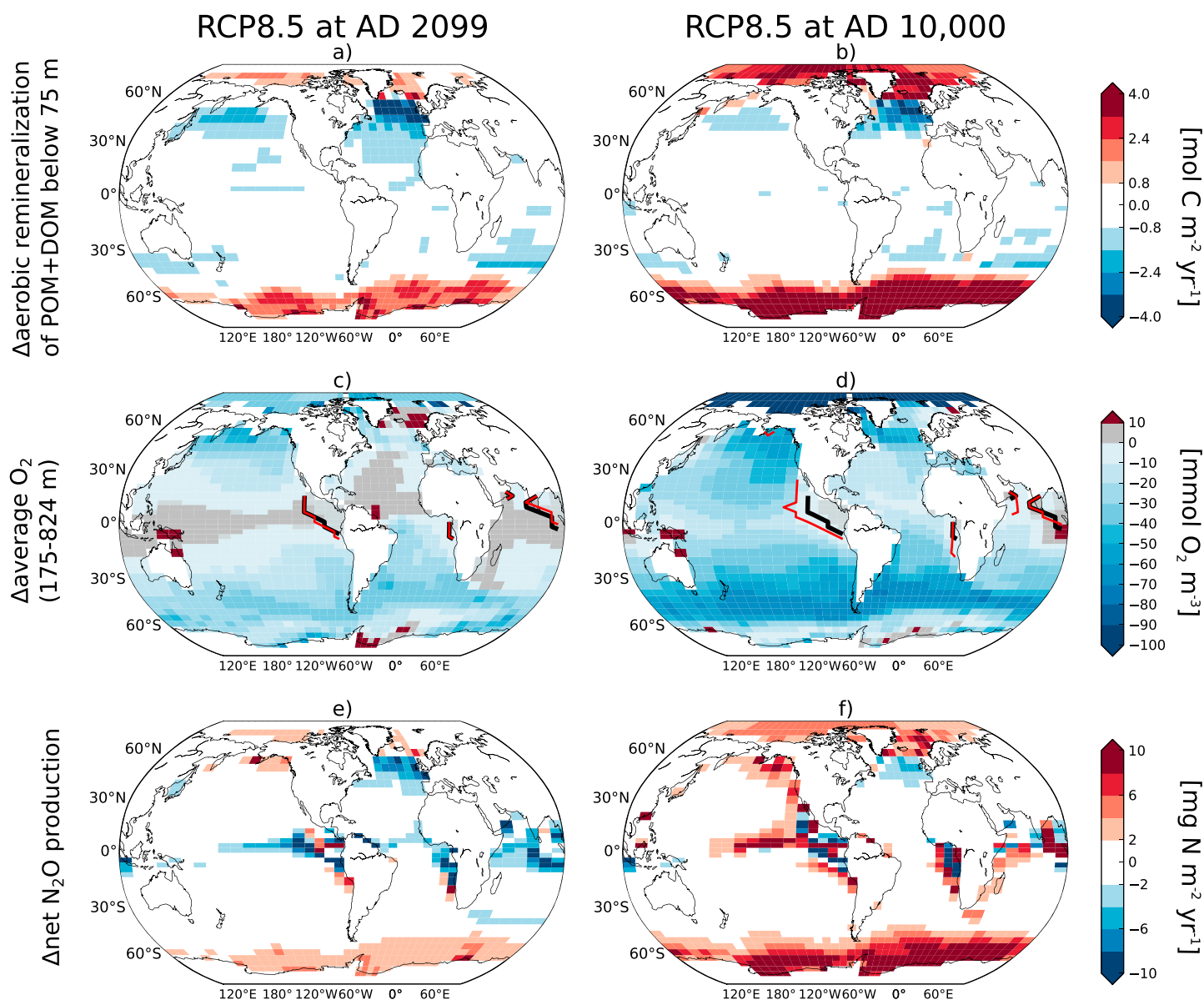


Figure 10. Maps of median changes (Δ) of variables of interest for the extended RCP8.5 scenario. (a, b) Aerobic remineralization of particulate and dissolved organic matter below the euphotic zone, (c, d) upper ocean (175–824 m) $[\text{O}_2]$, and (e, f) net N_2O production integrated over the entire water column. Results are for year 2099 minus 1990–2005 averaged time period (first column) and for year 10,000 minus 1990–2005 averaged time period (second column). Contour lines in Figures 10c and 10d mark the extent of waters with less than $5 \text{ mmol O}_2 \text{m}^{-3}$ for modern (black) conditions and at 2099 and 10,000 A.D. (red). Color bars apply to both time slices.

their distributions. As the Indo-Pacific MOC is enhanced under the new steady state, the deep ocean is better ventilated, except in the North Atlantic, where a shallower AMOC increases water mass age and nutrient concentrations in the deep.

Global export production and remineralization fluxes decrease till A.D. ~ 2200 , slowly recover thereafter and overshoot preindustrial levels at A.D. ~ 5000 (Figure 9b and Table D2). The long-term increase in export production is driven by higher biological export productivity in the Arctic and Southern Oceans due to reduced temperature and light limitation of productivity in response to warming and sea ice retreat. This results in correspondingly higher remineralization fluxes in high latitudes (Figures 10a and 10b). In contrast, no change or a decrease in export and remineralization is projected in other regions (Figures 10a and 10b). Negative anomalies in remineralization are most pronounced in the northern North Atlantic and also occur in the Atlantic,

Indian, and northern North Pacific. This is mainly a result of increased stratification and a concomitant increase in nutrient limitation of productivity, similarly as discussed by Steinacher et al. (2009). On global average, the decrease in the remineralization flux is largest when the MOC is lowest.

O₂ is affected by changing ocean physics, warming, and biogeochemistry. The global mean [O₂] decreases by a factor of 2 in the next 2,000 years and remains below preindustrial over the entire high GHG simulation (RCP8.5) (Figures 7, 9g, 10c, and 10d). These changes only emerge on multicentury to millennial timescales. By the end of the 21st century, the distribution of low O₂ water volumes has hardly changed (Figure 7b and Table D1). Deoxygenation peaks at year A.D. 4000 when deep water had sufficient time to age, to accumulate remineralized nutrients, and to integrate losses by oxygen consumption. In addition, warming causes O₂ loss due to changes in solubility (see also Battaglia & Joos, 2017 for process attribution).

The projected changes affect the distribution of low O₂ waters, and the volume of water holding low O₂ concentrations expands in the deep ocean. The volume of water with [O₂] <50 mmol O₂ m⁻³ increases by about a factor of 8, and the volume of water with [O₂] <5 mmol O₂ m⁻³ increases by more than a factor of 2 until A.D. 4000 (Table D1 and Figure 7). Under new steady state conditions, the respective volumes are still ~50% larger than today. Transiently, higher [O₂] is established in upper ocean equatorial waters where remineralization is lowered and ventilation increased compared to preindustrial. Under new steady state conditions, O₂ concentrations partly recover in much of the deep ocean as deep overturning is again enhanced. A lower O₂ solubility component (−43.0 mmol O₂ m⁻³) due to warming prevents global average [O₂] from recovering to preindustrial values, and negative [O₂] anomalies establish in the upper ocean. Also, negative [O₂] anomalies remain in the deep North Atlantic as a result of the shallower AMOC. The simulated O₂ changes are comparable to those by Schmittner et al. (2008 SRES A2 scenario over 2,000 years) who found global mean [O₂] concentrations to transiently decline by 30% and slowly recover thereafter and the suboxic volume to triple. Similar mechanisms, albeit different magnitudes, were reported by Yamamoto et al. (2015) for a 4 × CO₂ simulation over 2,000 years. Global mean [O₂] concentrations initially decrease but overshoot preindustrial levels after 1,500 years as overturning is enhanced. In their simulation, the volume of hypoxic waters increased initially and decreased thereafter. This results from sustained reductions in export production and shallower remineralization depth in response to increased temperatures in their study.

3.4.2. Drivers of N₂O Production Changes

The evolution of remineralization and [O₂] determines the evolution of marine N₂O production. Globally averaged N₂O production is projected to decrease over the 21st century (Figures 9f and 9h) in line with reductions in aerobic remineralization. The trend is reversed in the 22nd century, and projected N₂O production increases to reach a new steady state around A.D. 7000. Global N₂O production increases faster than global remineralization fluxes, highlighting the influence of changes in O₂ on the N₂O yield from aerobic remineralization. By the end of the 21st century, global N₂O production decreases by 0.33 (0.21 to 0.46) Tg N yr⁻¹ (median percentage change: 7.7%). N₂O production stabilizes at rates of 0.73 (0.56 to 0.98) Tg N yr⁻¹ (21%) higher than today. The air-sea flux of N₂O adjusts to changes in N₂O production with a time lag related to the exchange timescales between deep and surface ocean waters. The transient slow down of the overturning circulation manifests itself in a transient increase in the oceanic N₂O inventory (Figure 9i). Additional N₂O from biological production accumulates within the ocean when circulation slows, despite a decrease in net N₂O production. The prescribed increase in atmospheric pN₂O under the RCP scenarios leads to an increase in the ocean's N₂O solubility component and a corresponding perturbation in the air-sea N₂O flux.

At the global scale, nitrification (0.67 (0.47 to 0.93) Tg N yr⁻¹, 92%) dominates the long-term increase in N₂O production (Figure 9h). The O₂ dependency of nitrification-production, " $\beta^*f(\text{O}_2)$ term," 0.49 (0.24 to 0.82) Tg N yr⁻¹, 68%, contributes the most. Over the 21st century, on the other hand, the dependency on organic matter remineralization prevails.

Turning to spatial patterns of change, changes in N₂O production are small in large parts of the Pacific, Indian, and Atlantic but significant in eastern equatorial regions, along the coast of Africa and in high latitudes (Figures 10e and 10f). [O₂] in the upper ocean is projected to slightly increase in equatorial regions over the industrial period and the 21st century (Figure 10c), while changes in export and remineralization are small around the equator (Figure 10a). As a result, pronounced negative anomalies in N₂O production are projected in eastern equatorial regions by 2099 A.D. (Figure 10e). There, [O₂] concentrations in the thermocline are low (Figure 3b), and, in turn, the sensitivity of N₂O production to changes in O₂ is high (Figure 1c). By the time a new steady state has established, positive O₂ anomalies are much less abundant and negative O₂ anomalies

prevail (Figure 10d). These negative O_2 anomalies explain the pronounced positive production anomalies in the eastern equatorial Pacific and Indian and along the coast of southern Africa, as well as in the North Pacific by the end of the simulation. The long-term increase in N_2O production in the Southern Ocean and the Arctic is linked to the increase in productivity, related to sea ice retreat, and the decrease in O_2 in the high-latitude thermocline and deep ocean.

Global N_2O production from denitrification is projected to moderately change over the course of the simulation. Small increases or decreases are possible. Under new steady state conditions, the median is projected to increase slightly. This evolution results from a complex interplay of anaerobic remineralization of organic matter, and O_2 and N_2O concentrations, and is more difficult to disentangle (Figures 9d, 9g, and 9i). Spatially, denitrification fluxes show anomalies in the OMZs of the eastern tropical Pacific, Atlantic, and Indian Oceans. Transiently, new denitrifying regions establish in the deep North Pacific and parts of the deep Southern Ocean.

In summary, an increase in export production and aerobic remineralization of organic material leads to positive N_2O production anomalies in the Arctic and Southern Oceans and a decrease in export and remineralization to negative production anomalies in the northern Atlantic. In other regions, particularly those with intermediate to low $[O_2]$, N_2O production changes are mainly driven by changes in N_2O yield due to changes in $[O_2]$.

3.5. N_2O Climate Feedback

The simulated changes in marine N_2O emissions to the atmosphere will provide a feedback on radiative forcing and climate. We diagnose the resulting changes in radiative forcing from a simple one box model (assuming a constant perturbation lifetime of 109 years (Prather et al., 2015) and using the radiative forcing given by Etminan et al., 2016). The related transient feedback factor is expressed as radiative forcing per temperature change (Figure 9j). Simulated changes in N_2O emissions initially cause a negative feedback by the end of the 21st century ($-0.005 \text{ W m}^{-2} \text{ K}^{-1}$ for RCP8.5). By the time a new steady state establishes, higher N_2O emissions cause a positive feedback to climate change ($0.004 \text{ W m}^{-2} \text{ K}^{-1}$ for RCP8.5).

4. Discussion

We find that marine N_2O production and its changes are dominated by nitrification. The dominant role of nitrification to N_2O production has also been inferred from in situ concentration measurements in combination with observational water mass age tracers (Freing et al., 2012, ~93% from nitrification). Comparison to other global modeling studies is difficult. Denitrification has not been included explicitly, and the remaining parameter values are usually chosen to yield net N_2O production of $\sim 3.8 \text{ Tg N yr}^{-1}$. Gross, global denitrification fluxes in our study for the modern ocean are ~ 13 times larger than N_2O from nitrification; the net effect, however, may range from net negative ($-0.34 \text{ Tg N yr}^{-1}$) to slightly positive ($0.79 \text{ Tg N yr}^{-1}$), supporting the view that net N_2O production is dominated by nitrification. In response to anthropogenic warming, net N_2O production by denitrification in the probabilistic assessment makes up 7.8% of the net change.

Marine production and emissions of N_2O critically depend on remineralization fluxes and O_2 concentrations with highest sensitivities at O_2 concentrations below $\sim 80 \text{ mmol } O_2 \text{ m}^{-3}$ such as found in the Equatorial Pacific. The Bern3D model projects regionally slightly elevated O_2 concentrations in this environment by the end of the 21st century, while the global volume occupied by low O_2 waters remains almost unchanged on this timescale. These results are in line with many Earth System models considered in Cocco et al. (2013, their Figures 2 and 6). Schmidtke et al. (2017), on the other hand, inferred from O_2 measurements that the oxygen minimum zones in the Equatorial Pacific expanded over the last five decades. Bern3D simulates such an expansion in the upper ocean of the Equatorial Pacific only on longer timescales.

The projected decrease in global N_2O production by the end of the 21st century under RCP8.5 (0.33 (0.21 to 0.46) Tg N yr^{-1}) is comparable to what Martinez-Rey et al. (2015) have found ($0.41 \text{ Tg N yr}^{-1}$, their POMZ parameterization) for the IPSL Earth system model. While the global decrease by the end of the 21st century and underlying mechanisms are compatible between the two studies, models can differ in their regional response. In the Equatorial Pacific, for instance, Martinez-Rey et al. (2015) project higher remineralization rates and lower O_2 concentrations and therefore increased N_2O production by 2099 which is in contrast to our results. In Bern3D, this region shows positive N_2O production anomalies only on longer timescales.

Our long-term simulations project that marine N_2O emissions will eventually cause a small, positive feedback to climate change on millennial timescales. As such, they would tend to add to the positive feedback

associated with the terrestrial biosphere (B. Stocker et al., 2013). We find a much smaller sensitivity of N_2O emissions to climate change than proposed by Schmittner et al. (2008), who projected a doubling of N_2O production in response to an extended high greenhouse gas scenario (SRES A2).

Ice core records have revealed a positive climate feedback in Earth's history, with higher natural N_2O production and emissions in warmer climates both from the land and from the ocean (Schilt et al., 2014, 2010). In our simulations, this positive feedback in response to anthropogenic warming becomes evident in long-term projections as a result of deoxygenation and higher remineralization fluxes. On the short term, transient decreases in circulation determine decreases in remineralization fluxes which decrease N_2O production. Such decreases are also in line with paleomodeling studies, where transient decreases in the AMOC lead to transient decreases in N_2O emissions. The Younger-Dryas cold period (12.7–11.55 kyr B.P., Goldstein et al., 2003) or Dansgaard-Oeschger climate oscillations (modeled for the period 50–45 kyr B.P. in Schmittner & Galbraith, 2008) are examples of such changes in the past.

5. Caveats in Modeling Marine N_2O

Observations of N_2O concentrations reveal high variability which are not resolved in EMICS such as Bern3D nor in state-of-the-art Earth System Models. It is likely that N_2O production varies on small spatial and temporal scales together with the variable availability of organic matter and O_2 . Here we account for this subgrid-scale variability by introducing functions for the relative share of aerobic versus anaerobic remineralization and of N_2O production versus consumption by denitrification. This permits the three processes— N_2O production by nitrification and denitrification and consumption by denitrification—to co-occur within a single grid cell with low $[\text{O}_2]$. In this framework, a tight coupling between N_2O produced and consumed by denitrification emerges. Higher-resolution modeling studies are needed to confirm this finding. We also recall that vast areas of the ocean have not been sampled yet.

Potentially important feedback mechanisms have been neglected in this study. Imbalances within the N cycle (denitrification versus N_2 fixation) can feedback on export production and therefore impact long-term projections of N_2O and marine biogeochemistry. Remineralization rates are assumed to be constant in time, as there is a lack of information on this issue (see, e.g., Roth et al., 2014). Further, we prescribe constant stoichiometric ratios and do not account for anthropogenic nitrogen deposition.

Ocean sediments are not explicitly represented in this study. Thus, organic matter remineralization and N_2O production and consumption by nitrification and denitrification within the sediments as well as diffusive exchange of N_2O between sediment pore water and ocean waters are not modeled. We assumed that all organic matter falling to the seafloor is nitrified under aerobic conditions, likely biasing N_2O production by nitrification high at the seafloor. This has a small impact on simulated N_2O emissions in our coarse-resolution model as the associated N_2O production is small. Regarding denitrification, we assume zero net production/consumption for the sedimentary deposition flux. This assumption appears justified for the open ocean and for simplicity as N_2O concentration data show small near-bottom gradients but may be more problematic along continental margins. In such boundary regions, N_2O concentrations and thus mechanisms modulating N_2O production and consumption show strong spatial heterogeneity (Bourbonnais et al., 2017). Benthic denitrification may significantly affect near-bottom N_2O concentrations as benthic denitrification fluxes are large. Our ensemble yields an N loss by benthic denitrification of 131.0 (121.0–144.0) Tg N yr^{-1} , well within the range of published estimates (Yang & Gruber, 2016 70–300 Tg N yr^{-1}) and larger than N loss by denitrification in the open ocean. Future modeling work may address benthic denitrification and associated N_2O production and consumption explicitly.

In addition, we did not account for pH dependencies. Surface ocean pH is projected to drop by the end of the 21st century (mean of CMIP5 models is 0.31 for RCP8.5) as anthropogenically emitted CO_2 dissolves in the ocean. This would further decrease the direct availability of NH_3 over NH_4^+ ($\text{pK}_a = 9.25$ at 25°C), which serves as the actual substrate of nitrification. Nitrification rates have been shown to decline in short-term manipulative experiments with lower pH (Beman et al., 2011). How the N_2O yield responds is uncertain given the complex production pathways. Rees et al. (2016) found less N_2O production with decreasing pH in temperate and polar marine environments, and Frame et al. (2017) found higher N_2O yields with unaltered nitrification rates in a freshwater lake. How potentially slower rates affect equilibrium distributions and competition among different processes remains to be determined.

Controversy also exists around potential nitrification in the surface ocean and associated production of N_2O . N_2O production in the euphotic zone was excluded in our model formulation. Because AOBs are thought to be light inhibited (Ward, 2008), nitrification (and N_2O production) in the surface layer has long been ruled out. A compilation of open ocean measurements of the specific rate of surface nitrification in combination with global modeling by Yool et al. (2007) revealed that nitrification may account for half of the nitrate taken up by growing phytoplankton. In recent years, AOA have in fact been observed in the euphotic zone (Beman et al., 2012; Church et al., 2010) and within enrichment cultures and incubation experiments AOA have been shown to produce N_2O (Loescher et al., 2012; Santoro et al., 2011). Most studies quantifying global surface N_2O production, nevertheless, rely on N_2O concentrations measurements within the water column and air-sea and cross-thermocline flux parameterizations (Charpentier et al., 2010; Dore & Karl, 1996; Law & Ling, 2001; Morell et al., 2001). Large uncertainties exist in the extrapolation of instant, local gas exchange fluxes over annual timescales and globally (Freing et al., 2012). N_2O production in the euphotic zone would be hard to constrain within data assimilation efforts such as ours, as the imprint on N_2O in the water column is small due to fast outgassing (see also Zamora & Oschlies, 2014). As the total flux of N_2O to the atmosphere $10.5 \pm 1 \text{ Tg N yr}^{-1}$ is constrained by its atmospheric lifetime (123 years for preindustrial conditions, Prather et al., 2015) the room for surface production is not that large as we already require $4.6 (3.1 \text{ to } 6.1) \text{ Tg N yr}^{-1}$ from the ocean for preindustrial conditions. This would leave 5.9 Tg N yr^{-1} preindustrial emissions from land in line with IPCC AR5 estimates of $6.6 (3.3 \text{ to } 9.0) \text{ Tg N yr}^{-1}$. Nevertheless, extremes of the confidence intervals (3.1 from the ocean and 3.3 Tg N yr^{-1} from the land) would allow for up to 5.1 Tg N yr^{-1} from surface production.

6. Conclusion

We present a novel parameterization of marine nitrous oxide (N_2O) production and consumption for application in ocean biogeochemical and Earth System Models. A probabilistic, Bayesian framework is applied, relying on a 1,000-member model ensemble and a comprehensive set of diverse observational data. The framework is used to constrain model parameters, modern global and regional marine N_2O fluxes, and probabilistic projections over this century and the next 8,000 years.

Observations of dissolved N_2O within the water column and of surface partial pressure of N_2O are used as constraints. In addition, observation-derived, globally gridded data sets of natural radiocarbon and dissolved oxygen (O_2) are used to constrain modern ocean circulation and physical transport timescales, remineralization fluxes of organic matter, and oxygen concentrations. These environmental parameters exert a crucial control on marine N_2O production and emissions.

Earlier N_2O modeling in global ocean models interpreted the O_2 dependency of nitrification to represent N_2O production from denitrification. Here denitrification fluxes are represented explicitly and related stoichiometrically to remineralization fluxes of organic matter. This new approach permits evaluation with estimates of total nitrogen loss by denitrification from the marine environment and considers the mass balance of organic matter conversion. Modeled N_2O production by denitrification and environmental sensitivities depends on the availability of organic matter, dissolved N_2O , and dissolved O_2 . The median value and uncertainty range of the constrained global denitrification flux are consistent with independent estimates of total nitrogen loss. Globally, net denitrification fluxes make up 4.5% of modern N_2O production and are responsible for about 7.8% of projected production changes.

The confidence range in marine N_2O emissions from our probabilistic framework, $2.8\text{--}5.9 \text{ Tg N yr}^{-1}$, is narrower than summarized in the latest report of the Intergovernmental Panel on Climate Change (IPCC), $1.8\text{--}9.4 \text{ Tg N yr}^{-1}$, while our constrained median of 4.3 Tg N yr^{-1} is higher than the IPCC best guess estimate of 3.8 Tg N yr^{-1} (Ciais et al., 2013). In response to human-made global warming and increased concentrations of greenhouse gases, we project marine N_2O production to first decrease by 7.7% over the 21st century in a business-as-usual scenario. This results from projected decreases in circulation and associated reductions in the export and remineralization of organic matter. For sustained anthropogenic forcing, the global marine oxygen inventory is reduced by a factor of 2 within the next two millennia with potential for far-reaching environmental consequences. Marine production of N_2O is projected to eventually become 21% higher than for today in response to widespread deoxygenation and higher remineralization fluxes. As such, marine N_2O emissions constitute a small, positive feedback to climate change on millennial timescales. Our simulations reveal intricate interactions between the marine carbon cycle, N_2O , oxygen, and climate.

Appendix A: Remineralization of Particulate Organic Matter

This appendix details the calculation of the remineralization of particulate organic matter (POP) in the Bern3D model. Biological productivity within the euphotic zone is a function of temperature, light availability, phosphate, and iron following Doney et al. (2006). One third of production is exported as POP and is remineralized instantaneously in the water column beneath. We apply the empirical power law profile of Martin et al. (1987) for both aerobic and anaerobic remineralization but with different scaling factors for aerobic ($\alpha_i = \alpha_{\text{aerob}}$) and anaerobic ($\alpha_i = \alpha_{\text{denit}}$) remineralization. The general form of the power law profile is

$$F_{x,y}(z_k) = F_{x,y}(z_{k-1}) \cdot \left(\frac{z_k}{z_{k-1}} \right)^{\alpha_i}, \quad \text{for } z > z_0. \quad (\text{A1})$$

$F_{x,y}(z_k)$ ($\text{mmol P m}^{-2} \text{s}^{-1}$) is the downward particle flux per unit area evaluated at the bottom of the grid cell (z_k) with longitude, latitude, and depth indices x , y , and k , respectively. z_0 is the depth of the euphotic zone and $F_{x,y}(z_0)$ is the export flux out of the euphotic zone taken as initial flux. The index k is taken to increase with depth.

We assume that the O_2 concentration within a grid cell varies around a modeled mean concentration such that aerobic and anaerobic remineralization may co-occur within the same grid cell. The fractions of DOP and POP that follow the aerobic path are (p_1), and the fraction that follows the anaerobic remineralization path is ($1-p_1$), where p_1 is a function of $[\text{O}_2]$. This yields for the flux of POP at depth k

$$F_{x,y}(z_k) = F_{x,y}(z_{k-1}) \cdot \left(p_1([\text{O}_2]) \left(\frac{z_k}{z_{k-1}} \right)^{\alpha_{\text{aerob}}} + (1 - p_1([\text{O}_2])) \left(\frac{z_k}{z_{k-1}} \right)^{\alpha_{\text{denit}}} \right), \quad \text{for } z > z_0. \quad (\text{A2})$$

The change in the POP flux with depth for aerobic remineralization within grid cell x , y , and k is then given by (omitting x and y for clarity)

$$\Delta F_{\text{aerob}}(z_k) = p_1([\text{O}_2(k)]) \cdot F(z_{k-1}) \cdot \left(1 - \left(\frac{z_k}{z_{k-1}} \right)^{\alpha_{\text{aerob}}} \right). \quad (\text{A3})$$

For anaerobic remineralization it is given by

$$\Delta F_{\text{denit}}(z_k) = (1 - p_1([\text{O}_2(k)])) \cdot F(z_{k-1}) \cdot \left(1 - \left(\frac{z_k}{z_{k-1}} \right)^{\alpha_{\text{denit}}} \right). \quad (\text{A4})$$

(p_1) is given by an error function (Figure 1b). This function depends on the mean modeled O_2 concentration, $\text{O}_2(x,y,k)$

$$p_1([\text{O}_2]) = 0.5 \cdot \left(1 + \text{erf} \frac{[\text{O}_2(x,y,k)] - \mu}{\sigma \cdot \sqrt{2}} \right). \quad (\text{A5})$$

The error function (erf) varies between -1 and $+1$. μ ($6 \text{ mmol O}_2 \text{ m}^{-3}$) corresponds to the O_2 concentration where erf is zero and p_1 equals 0.5 (see Figure 1b). σ ($0.7 \text{ mmol O}_2 \text{ m}^{-3}$) is the standard deviation of the distribution. At low $[\text{O}_2]$, p_1 is zero and only denitrification occurs. p_1 increases from zero to one as the mean O_2 concentration in a grid cell increases from about 4.4 to 7.4 $\text{mmol O}_2 \text{ m}^{-3}$. Within this O_2 concentration range ($\sim \mu \pm 2\sigma$) both denitrification and aerobic remineralization (including nitrification) co-occur. p_1 is one for higher O_2 concentrations such that only the aerobic path is followed.

The parameter values of the function p_1 are selected based on sensitivity experiments. While values of α_{aerob} and α_{denit} are varied within the Monte Carlo approach, the parameters of p_1 are not varied. This is to limit the number of free parameters and as variations in μ and σ and variations in α_i that have compensating influence on remineralization.

The remineralization of DOP is assigned to aerobic and anaerobic conditions with the same function (p_1). The organic flux reaching the seafloor is remineralized in the deepest box. The O_2 demand for complete aerobic remineralization ($r_{\text{O}_2:\text{P}}$) is $170 \frac{\text{mol O}_2}{\text{mol PO}_4}$ and includes nitrification. There is no O_2 consumption during denitrification. The O_2 consumption term (or aerobic remineralization, $\text{mmol O}_2 \text{ m}^{-3} \text{s}^{-1}$) then is

$$J(\text{O}_2) = 170 \cdot \left(\frac{\Delta F_{\text{aerob}}(z_k)}{z_{k-1} - z_k} + \frac{[\text{DOP}] \cdot p_1}{1.5 \text{ years}} \right). \quad (\text{A6})$$

Fixed stoichiometric ratios are used to convert biological P fluxes into carbon (C) and alkalinity (Alk) fluxes for both aerobic and anaerobic remineralization (P:Alk:C = 1:17:117). Alkalinity fluxes are not adjusted under anaerobic conditions for reasons of mass conservation as the model does not include N₂ fixation.

Appendix B: N₂O Production Versus Consumption

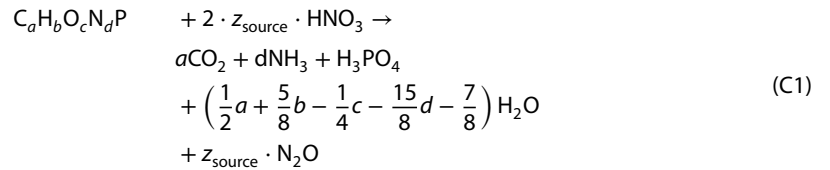
The function separating N₂O production and consumption at low O₂ is defined as

$$p_2([O_2]) = 0.5 \cdot \left(1 + \operatorname{erf} \frac{[O_2] - (\mu - \text{offset})}{\sigma \cdot \sqrt{2}} \right). \quad (\text{B1})$$

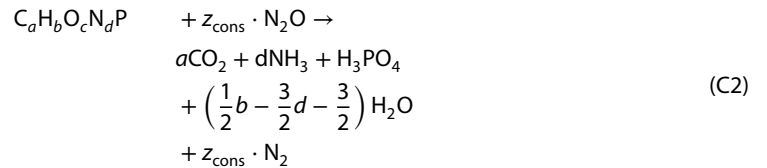
p_2 is equal to the function separating aerobic and anaerobic conditions, except that it is shifted toward lower O₂ values by an offset (Figure 1b).

Appendix C: Stoichiometry for Denitrification With N₂O as Obligate Intermediate Product

To develop formulations of N₂O production by denitrification, we establish the stoichiometric relationships between N₂O produced (z_{source}) or consumed (z_{cons}) per molecule P released by anaerobic remineralization. The stoichiometric relationship with N₂O as the direct and only obligate intermediate product is—after Paulmier et al. (2009)



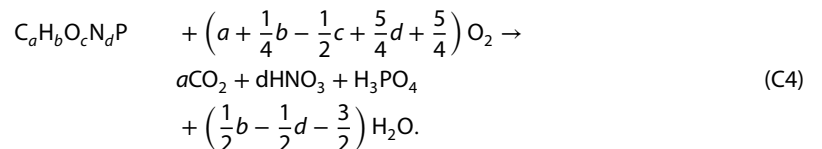
for N₂O production and



for N₂O consumption. It follows that

$$\begin{aligned} z_{\text{source}} &= \left(\frac{1}{2}a + \frac{1}{8}b - \frac{1}{4}c - \frac{3}{8}d + \frac{5}{8} \right), \\ z_{\text{cons}} &= \left(2a + \frac{1}{2}b - c - \frac{3}{2}d + \frac{5}{2} \right). \end{aligned} \quad (\text{C3})$$

How much N₂O is produced (z_{source}) and how much consumed (z_{cons}) per P remineralized therefore depends on the composition of the organic matter (a , b , c , and d). As most global biogeochemical models, the standard version of the Bern3D model prescribes only the C:P ($a = 117$) and N:P ($d = 16$) ratios without specifying the assumed H and O content of the organic matter. However, the terms $(\frac{1}{8}b - \frac{1}{4}c)$ and $(\frac{1}{2}b - c)$ in equation (C3) can be consistently inferred from the oxygen demand of complete aerobic remineralization, set to O₂:P = −170 in the Bern3D model. Complete aerobic remineralization of organic matter (including nitrification) follows (Paulmier et al., 2009):



Thus, $(a + \frac{1}{4}b - \frac{1}{2}c + \frac{5}{4}d + \frac{5}{4}) = 170$ or equivalently $\frac{1}{8}b - \frac{1}{4}c = 15.875$ and $\frac{1}{2}b - c = 63.5$ in Bern3D. This yields $z_{\text{source}} = 69$ and $z_{\text{cons}} = 276$ for the given C:P and N:P ratios and the given oxygen demand of complete aerobic remineralization. Different compositions of organic matter have been reported. Assuming classical Redfield (1963) stoichiometry of C₁₀₆H₂₆₃O₁₁₀N₁₆P would imply that $z_{\text{source}} = 53$ and $z_{\text{cons}} = 212$. The stoichiometry

proposed by Anderson (1995) of $C_{106}H_{175}O_{42}N_{16}P$ would result in $z_{\text{source}} = 59$ and $z_{\text{cons}} = 236$. Here we rely on stoichiometric values derived from the analysis of thermocline and deep water composition by Anderson and Sarmiento (1994), which results in 30% and 15% higher values for these stoichiometric ratios.

Appendix D: Summary of Numerical Results

In Figure D1, the cumulative weight and a histogram of the skill scores are shown. In the Bern3D model, the chosen formulations of N_2O production and consumption can lead to very high point sources close to the

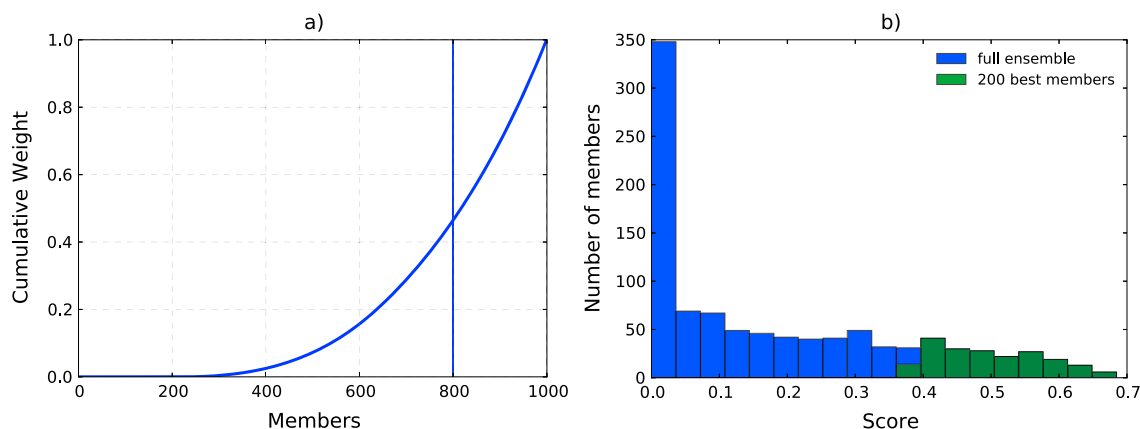


Figure D1. (a) Cumulative weight and (b) histogram of the skill scores. The top 200 ensemble members, chosen for the extended long-term projections, represent 54% of the total weight of all 1,000 members.

Table D1

Modeled and Observed Volumes of three Different Low O_2 Regimes

	Volume (10^{15} m^3)		
	$O_2 < 80 \text{ mmol m}^{-3}$	$O_2 < 50 \text{ mmol m}^{-3}$	$O_2 < 5 \text{ mmol m}^{-3}$
This study ^a (1990–2005)	144.9 (125.2 to 170.5)	68.5 (61.1 to 78.4)	7.1 (6.4 to 8.1)
WOA09 ^b (WOA13 ^c on B3D grid)	126 (127.7)	60.4 (64.6)	2.43 (1.4)
<i>From Cocco et al. (2013)</i>			
BCM-C 1990s	137	68.4	19.9
IPSL 1990s	38.9	18.5	1.01
UVIC2-8 1990s	67.9	32.9	4.91
CSM1.4 1990s	33.3	18.1	5.44
CCSM3 1990s	38.6	22.5	6.55
GFDL 1990s	153	105	39.9
MPIP 1990s	154	93.6	35.7
<i>RCP2.6</i>			
This study A.D. 2099	153.0 (135.0 to 177.0)	73.0 (66.4 to 83.1)	7.37 (6.51 to 8.33)
This study A.D. 4000	252.0 (174.0 to 337.0)	99.6 (75.5 to 137.0)	8.5 (7.54 to 9.3)
This study A.D. 10,000	120.0 (111.0 to 135.0)	61.7 (59.0 to 65.7)	7.01 (6.46 to 7.8)
<i>RCP8.5</i>			
This study A.D. 2099	157.0 (141.0 to 182.0)	76.5 (69.9 to 86.5)	7.31 (6.24 to 8.34)
This study A.D. 4000	777.0 (731.0 to 813.0)	555.0 (468.0 to 613.0)	18.6 (15.7 to 30.7)
This study A.D. 10,000	201.0 (185.0 to 223.0)	106.0 (99.9 to 113.0)	11.9 (10.4 to 13.5)

^aValues for this study include the median and the $\pm 1\sigma$ range. ^bFrom Cocco et al. (2013) (including Bianchi et al., 2012 correction). ^cIncluding Bianchi et al. (2012) correction.

Table D2
Summary of Results

Variable (unit)	Modern (1990–2005)	RCP2.6 Δ in A.D. 2099	RCP2.6 Δ in A.D. 10,000 ^a	RCP8.5 Δ in A.D. 2099	RCP8.5 Δ in A.D. 10,000 ^a
Global mean SAT (°C)	16.2 (16.1 to 16.4)	1.53 (1.49 to 1.55)	1.8 (1.62 to 1.91)	4.89 (4.77 to 4.99)	11.1 (10.9 to 11.2)
Global mean ocean T (°C)	4.26 (3.97 to 4.5)	0.343 (0.336 to 0.353)	1.55 (1.42 to 1.71)	0.651 (0.644 to 0.657)	7.24 (7.16 to 7.29)
AMOC (Sv)	16.3 (15.5 to 17.0)	−2.18 (−2.58 to −1.83)	2.97 (2.56 to 3.49)	−6.8 (−7.24 to −6.42)	1.52 (1.2 to 1.8)
Indo-Pacific MOC (Sv)	13.3 (12.8 to 13.9)	−2.59 (−2.2 to −2.82)	2.25 (2.38 to 2.07)	−5.79 (−5.5 to −6.08)	3.55 (3.9 to 3.36)
Global mean O ₂ (mmol m ^{−3})	155.0 (148.0 to 163.0)	−4.14 (−4.67 to −3.53)	6.8 (4.71 to 10.6)	−7.34 (−7.94 to −6.65)	−20.1 (−25.3 to −16.3)
N inventory solubility (Tg N)	427.0 (425.0 to 429.0)	10.9 (10.8 to 11.2)	77.3 (76.4 to 78.0)	19.6 (19.2 to 20.1)	212.0 (208.0 to 216.0)
N inventory biology (Tg N)	411.0 (271.0 to 552.0)	5.92 (3.61 to 9.81)	−42.2 (−69.2 to −26.8)	10.1 (6.31 to 15.9)	−31.2 (−50.8 to −6.7)
Export production (Gt C yr ^{−1})	9.88 (9.19 to 10.6)	−0.142 (−0.16 to −0.105)	0.761 (0.669 to 0.87)	−0.545 (−0.596 to −0.476)	0.612 (0.55 to 0.716)
Aerobic remin. fluxes (Gt C yr ^{−1})	19.7 (18.2 to 21.2)	−0.26 (−0.311 to −0.157)	1.88 (1.68 to 2.14)	−1.37 (−1.54 to −1.17)	1.68 (1.51 to 1.92)
Denitrification (10 ^{−3} Gt C yr ^{−1})	48.3 (30.3 to 67.7)	−0.868 (−1.34 to −0.284)	4.01 (2.61 to 5.51)	−2.68 (−4.4 to −1.34)	16.6 (9.16 to 26.3)
Net N ₂ O prod. (Tg N yr ^{−1})	4.51 (3.03 to 6.08)	−0.0628 (−0.0915 to −0.0367)	0.345 (0.225 to 0.475)	−0.33 (−0.456 to −0.211)	0.732 (0.559 to 0.981)
N ₂ O emissions (Tg N yr ^{−1})	4.33 (2.84 to 5.87)	−0.0325 (−0.00263 to −0.0643)	0.509 (0.645 to 0.389)	−0.567 (−0.427 to −0.714)	0.898 (1.15 to 0.72)
N ₂ O prod. α (Tg N yr ^{−1}) ^b	2.2 (0.691 to 3.71)	−0.025 (−0.0499 to −0.00693)	0.195 (0.0631 to 0.334)	−0.154 (−0.258 to −0.0466)	0.173 (0.0603 to 0.298)
N ₂ O prod. $\beta^*f(O_2)$ (Tg N yr ^{−1}) ^c	1.82 (0.874 to 3.41)	−0.0335 (−0.0639 to −0.0105)	0.0863 (0.0409 to 0.152)	−0.1 (−0.172 to −0.0437)	0.489 (0.237 to 0.824)
Net N ₂ O from denit. (Tg N yr ^{−1})	0.201 (−0.339 to 0.792)	0.00209 (−0.0278 to 0.028)	0.0441 (−0.00447 to 0.102)	−0.0673 (−0.159 to 0.0162)	0.0587 (−0.0799 to 0.195)
Feedback (10 ^{−3} W m ^{−2} K ^{−1}) ^d	−6.34 (−7.59 to −5.43)	−6.73 (−8.32 to −5.45)	6.95 (4.41 to 9.43)	−4.83 (−5.94 to −3.9)	3.69 (2.81 to 4.93)

Note. Modern reference median values (1990–2005) and $\pm 1\sigma$ ranges of the variables of interest, the changes (Δ) by the end of the 21st century, and the changes for new steady state conditions by A.D. 10,000 for the two scenarios (RCP2.6 and RCP8.5). The values correspond to the time series in Figure 9.

^aThe changes for A.D. 10,000 conditions are based on a reduced ensemble, including only the 200 members with the highest skill (S_m). ^bProduction from α refers to the constant nitrification yield.

^cProduction from $\beta^*f(O_2)$ refers to the O₂-dependent nitrification yield. ^dThe feedback factor is expressed relative to preindustrial values.

surface which in turn can lead to numerical oscillations from the advection scheme (neighboring cells in horizontal direction without these high sources have negative $[\text{N}_2\text{O}]$ or $[\text{N}_2\text{O}_\beta]$ lower than its solubility component; see section 2.4 for the definition of $[\text{N}_2\text{O}_\beta]$). In the skill assessment, these grid cells are excluded. This concerns $\sim 1\%$ of the oceanic grid cells. For the calculation of median values and ranges all cells are considered. Skill scores computed by including these cells yield indistinguishable results compared to excluding these cells.

Table D1 summarizes modeled and observed volumes of three different low O_2 regimes, and Table D2 summarizes the median values and confidence intervals for critical variables addressed in the main text.

Acknowledgments

This work was supported by the Swiss National Science Foundation (200020_159563). We thank two anonymous reviewers and Sara Mikaloff Fletcher for their constructive and thorough reviews and comments which improved the manuscript. Many thanks to Niki Gruber, Patrik Pfister, Sebastian Lienert, Ece Satar, Aurich Jeltsch-Thoemmes, and Angelique Hameau for fruitful discussions. Many thanks to Annette Kock and Herman Bange for generating and distributing the MEMENTO Database. The MEMENTO database is administered by the Kiel Data Management Team at GEOMAR Helmholtz Centre for Ocean Research and supported by the German BMBF project SOPRAN (Surface Ocean Processes in the Anthropocene, <http://sopran.pangaea.de>). The database is accessible through the MEMENTO webpage: <https://memento.geomar.de>. All other data used in this study are listed in the references. Model output is available upon request to the corresponding author (battaglia@climate.unibe.ch).

References

- Anderson, L. A. (1995). On the hydrogen and oxygen content of marine phytoplankton. *Deep Sea Research Part I: Oceanographic Research Papers*, 42(11), 1675–1680. [https://doi.org/10.1016/0967-0637\(95\)00072-E](https://doi.org/10.1016/0967-0637(95)00072-E)
- Anderson, L. A., & Sarmiento, J. L. (1994). Redfield ratios of remineralization determined by nutrient data analysis. *Global Biogeochemical Cycles*, 8, 65–80.
- Arévalo-Martínez, D. L., Kock, A., Löscher, C. R., Schmitz, R. A., & Bange, H. W. (2015). Massive nitrous oxide emissions from the tropical South Pacific Ocean. *Nature Geoscience*, 8, 530–533. <https://doi.org/10.1038/ngeo2469>
- Arévalo-Martínez, D. L., Kock, A., Löscher, C. R., Schmitz, R. A., Stramma, L., & Bange, H. W. (2016). Influence of mesoscale eddies on the distribution of nitrous oxide in the eastern tropical South Pacific. *Biogeosciences*, 13(4), 1105–1118. <https://doi.org/10.5194/bg-13-1105-2016>
- Babbín, A. R., Bianchi, D., Jayakumar, A., & Ward, B. B. (2015). Rapid nitrous oxide cycling in the suboxic ocean. *Science*, 348(6239), 1127–1129. <https://doi.org/10.1126/science.aaa8380>
- Bakker, P., Schmittner, A., Lenaerts, J. T. M., Abe-Ouchi, A., Bi, D., van den Broeke, M. R., ... Yin, J. (2016). Fate of the Atlantic Meridional Overturning Circulation: Strong decline under continued warming and Greenland melting. *Geophysical Research Letters*, 43, 12,252–12,260. <https://doi.org/10.1002/2016GL070457>
- Bange, H. W. (2008). Chapter 2: Gaseous nitrogen compounds (NO , N_2O , N_2 , NH_3) in the Ocean. In D. G. Capone, et al. (Eds.), *Nitrogen in the marine environment* (2nd ed., pp. 51–94). San Diego, CA: Academic Press. <https://doi.org/10.1016/B978-0-12-372522-6.00002-5>
- Battaglia, G., & Joos, F. (2017). Hazards of decreasing marine oxygen: The near-term and millennial-scale benefits of meeting the Paris climate targets. *Earth System Dynamics Discussions*, 2017, 1–21. <https://doi.org/10.5194/esd-2017-90>
- Battaglia, G., Steinacher, M., & Joos, F. (2016). A probabilistic assessment of calcium carbonate export and dissolution in the modern ocean. *Biogeosciences*, 13(9), 2823–2848. <https://doi.org/10.5194/bg-13-2823-2016>
- Beman, J. M., Chow, C.-E., King, A. L., Feng, Y., Fuhrman, J. A., Andersson, A., ... Hutchins, D. A. (2011). Global declines in oceanic nitrification rates as a consequence of ocean acidification. *Proceedings of the National Academy of Sciences*, 108(1), 208–213. <https://doi.org/10.1073/pnas.1011053108>
- Beman, J. M., Popp, B. N., & Alford, S. E. (2012). Quantification of ammonia oxidation rates and ammonia-oxidizing archaea and bacteria at high resolution in the Gulf of California and eastern tropical North Pacific Ocean. *Limnology and Oceanography*, 57(3), 711–726. <https://doi.org/10.4319/lo.2012.57.3.0711>
- Bianchi, D., Dunne, J. P., Sarmiento, J. L., & Galbraith, E. D. (2012). Data-based estimates of suboxia, denitrification, and N_2O production in the ocean and their sensitivities to dissolved O_2 . *Global Biogeochemical Cycles*, 26, GB2009. <https://doi.org/10.1029/2011gb004209>
- Bopp, L., Resplandy, L., Orr, J. C., Doney, S. C., Dunne, J. P., Gehlen, M., ... Vichi, M. (2013). Multiple stressors of ocean ecosystems in the 21st century: Projections with CMIP5 models. *Biogeosciences*, 10(10), 6225–6245. <https://doi.org/10.5194/bg-10-6225-2013>
- Bourbonnais, A., Letscher, R. T., Bange, H. W., Échevin, V., Larkum, J., Mohn, J., ... Altabet, M. A. (2017). N_2O production and consumption from stable isotopic and concentration data in the Peruvian coastal upwelling system. *Global Biogeochemical Cycles*, 31, 678–698. <https://doi.org/10.1002/2016GB005567>
- Breider, F., Yoshikawa, C., Abe, H., Toyoda, S., & Yoshida, N. (2015). Origin and fluxes of nitrous oxide along a latitudinal transect in western North Pacific: Controls and regional significance. *Global Biogeochemical Cycles*, 29, 1014–1027. <https://doi.org/10.1002/2014GB004977>
- Butler, J. H., Elkins, J. W., Thompson, T. M., & Egan, K. B. (2000). Tropospheric and dissolved N_2O of the West Pacific and East Indian Oceans during the El Niño–Southern Oscillation event of 1987. *Journal of Geophysical Research*, 94, 14,865–14,877. <https://doi.org/10.1029/JD094iD12p14865>
- Castro-Gonzalez, M., & Farias, L. (2004). N_2O cycling at the core of the oxygen minimum zone off northern Chile. *Marine Ecology Progress Series*, 280, 1–11. <https://doi.org/10.3354/meps280001>
- Charpentier, J., Farias, L., & Pizarro, O. (2010). Nitrous oxide fluxes in the central and eastern South Pacific. *Global Biogeochemical Cycles*, 24, GB3011. <https://doi.org/10.1029/2008GB003388>
- Charpentier, J., Farias, L., Yoshida, N., Boontanon, N., & Raimbault, P. (2007). Nitrous oxide distribution and its origin in the central and eastern South Pacific Subtropical Gyre. *Biogeosciences*, 4(5), 729–741. <https://doi.org/10.5194/bg-4-729-2007>
- Church, M. J., Wai, B., Karl, D. M., & DeLong, E. F. (2010). Abundances of crenarchaeal amoA genes and transcripts in the Pacific Ocean. *Environmental Microbiology*, 12(3), 679–688. <https://doi.org/10.1111/j.1462-2920.2009.02108.x>
- Ciais, P., Sabine, C., Bala, G., Bopp, L., Brovkin, V., Canadell, J., ... Thornton, P. (2013). Chapter 6: Carbon and other biogeochemical cycles. In *Climate Change 2013: The Physical Science Basis. Working Group I Contribution to the Fifth Assessment Report of the Intergovernmental Panel on Climate Change*, 7, Final Draft. June 2013.
- Cocco, V., Joos, F., Steinacher, M., Frölicher, T. L., Bopp, L., Dunne, J., ... Tjiputra, J. (2013). Oxygen and indicators of stress for marine life in multi-model global warming projections. *Biogeosciences*, 10(3), 1849–1868. <https://doi.org/10.5194/bg-10-1849-2013>
- Cohen, Y., & Gordon, L. I. (1979). Nitrous oxide production in the Ocean. *Journal of Geophysical Research*, 84(C1), 347–353. <https://doi.org/10.1029/JC084iC01p00347>
- Devol, A. H. (2008). Chapter 6: Denitrification including anammox, (2nd ed.). In D. G. Capone, et al. (Eds.), *Nitrogen in the marine environment* (pp. 263–301). San Diego, CA: Academic Press. <https://doi.org/10.1016/B978-0-12-372522-6.00006-2>
- DeVries, T., Deutsch, C., Rafter, P. A., & Primeau, F. (2013). Marine denitrification rates determined from a global 3-D inverse model. *Biogeosciences*, 10(4), 2481–2496. <https://doi.org/10.5194/bg-10-2481-2013>
- Doney, S. C., Lindsay, K., Fung, I., & John, J. (2006). Natural variability in a stable, 1000-yr global coupled climate-carbon cycle simulation. *Journal of Climate*, 19(13), 3033–3054. <https://doi.org/10.1175/JCLI3783.1>

- Dore, J. E., & Karl, D. M. (1996). Nitrification in the euphotic zone as a source for nitrite, nitrate, and nitrous oxide at Station ALOHA. *Limnology and Oceanography*, 41(8), 1619–1628. <https://doi.org/10.4319/lo.1996.41.8.1619>
- Eby, M., Weaver, A. J., Alexander, K., Zickfeld, K., Abe-Ouchi, A., Cimadoribus, A. A., ... Zhao, F. (2013). Historical and idealized climate model experiments: An intercomparison of Earth system models of intermediate complexity. *Climate of the Past*, 9(3), 1111–1140. <https://doi.org/10.5194/cp-9-1111-2013>
- Etminan, M., Myhre, G., Highwood, E. J., & Shine, K. P. (2016). Radiative forcing of carbon dioxide, methane, and nitrous oxide: A significant revision of the methane radiative forcing. *Geophysical Research Letters*, 43, 12,614–12,623. <https://doi.org/10.1002/2016GL071930>
- Frame, C., Deal, E., Nevison, C. D., & Casciotti, K. L. (2014). N₂O production in the eastern South Atlantic: Analysis of N₂O stable isotopic and concentration data. *Global Biogeochemical Cycles*, 28, 1262–1278. <https://doi.org/10.1002/2013GB004790>. Received
- Frame, C. H., & Casciotti, K. L. (2010). Biogeochemical controls and isotopic signatures of nitrous oxide production by a marine ammonia-oxidizing bacterium. *Biogeosciences*, 7(9), 2695–2709. <https://doi.org/10.5194/bg-7-2695-2010>
- Frame, C. H., Lau, E., Nolan, E. J., Goepfert, T. J., Lehmann, M. F. (2017). Acidification enhances hybrid N₂O production associated with aquatic ammonia-oxidizing microorganisms. *Frontiers in Microbiology*, 7, 2104. <https://doi.org/10.3389/fmicb.2016.02104>
- Francis, C. A., Roberts, K. J., Beman, J. M., Santoro, A. E., & Oakley, B. B. (2005). Ubiquity and diversity of ammonia-oxidizing archaea in water columns and sediments of the ocean. *Proceedings of the National Academy of Sciences of the United States of America*, 102(41), 14,683–14,688.
- Freng, A., Wallace, D. W. R., & Bange, H. W. (2012). Global oceanic production of nitrous oxide. *Philosophical Transactions of the Royal Society B: Biological Sciences*, 367(1593), 1245–1255. <https://doi.org/10.1098/rstb.2011.0360>
- Garcia, H. E., Locarnini, R. A., Boyer, T. P., Antonov, J. I., Baranova, O. K., Zweng, M. M., ... Johnson, D. R. (2014). World Ocean Atlas 2013, volume 3: Dissolved oxygen, apparent oxygen utilization, and oxygen saturation. In S. Levitus, & A. Mishonov Technical, *NOAA Atlas NESDIS 75* (p. 27).
- Gerber, M., & Joos, F. (2013). An Ensemble Kalman Filter multi-tracer assimilation: Determining uncertain ocean model parameters for improved climate-carbon cycle projections. *Ocean Modelling*, 64, 29–45. <https://doi.org/10.1016/j.ocemod.2012.12.012>
- Gilly, W. F., Beman, J. M., Litvin, S. Y., & Robison, B. H. (2013). Oceanographic and biological effects of shoaling of the oxygen minimum zone. *Annual Review of Marine Science*, 5(1), 393–420. <https://doi.org/10.1146/annurev-marine-120710-100849>
- Goldstein, B., Joos, F., & Stocker, T. F. (2003). A modeling study of oceanic nitrous oxide during the Younger Dryas cold period. *Geophysical Research Letters*, 30(2), 1092. <https://doi.org/10.1029/2002GL016418>
- Goreau, T. J., Kaplan, W. A., & Wofsy, S. C. (1980). Production of NO₂⁻ and N₂O by nitrifying bacteria at reduced concentrations of oxygen. *Applied and Environmental Microbiology*, 40(3), 526–532.
- Griffies, S. M. (1998). The Gent-McWilliams skew flux. *Journal of Physical Oceanography*, 28(5), 831–841. [https://doi.org/10.1175/1520-0485\(1998\)028<0831:TGMSF>2.0.CO;2](https://doi.org/10.1175/1520-0485(1998)028<0831:TGMSF>2.0.CO;2)
- Gruber, N. (2008). Chapter 1—The marine nitrogen cycle: Overview and challenges. In D. G. Capone, et al. (Eds.), *Nitrogen in the marine environment* (2nd ed., pp. 1–50). San Diego, CA: Academic Press. <https://doi.org/10.1016/B978-0-12-372522-6.00001-3>
- Ji, Q., Babbitt, A. R., Jayakumar, A., Oleynik, S., & Ward, B. B. (2015). Nitrous oxide production by nitrification and denitrification in the Eastern Tropical South Pacific oxygen minimum zone. *Geophysical Research Letters*, 42, 10,755–10,764. <https://doi.org/10.1002/2015GL066853>
- Jin, X., & Gruber, N. (2003). Offsetting the radiative benefit of ocean iron fertilization by enhancing N₂O emissions. *Geophysical Research Letters*, 30(24), 2249. <https://doi.org/10.1029/2003GL018458>
- Kalnay, E., Kanamitsu, M., Kistler, R., Collins, W., Deaven, D., Gandin, L., ... Joseph, D. (1996). The NCEP/NCAR 40-year reanalysis project. *Bulletin of the American Meteorological Society*, 77(3), 437–471. [https://doi.org/10.1175/1520-0477\(1996\)077<0437:TNYRP>2.0.CO;2](https://doi.org/10.1175/1520-0477(1996)077<0437:TNYRP>2.0.CO;2)
- Kartal, B., Kuypers, M. M. M., Lavik, G., Schalk, J., Op den Camp, H. J. M., Jetten, M. S. M., & Strous, M. (2007). Anammox bacteria disguised as denitrifiers: Nitrate reduction to dinitrogen gas via nitrite and ammonium. *Environmental Microbiology*, 9(3), 635–642. <https://doi.org/10.1111/j.1462-2920.2006.01183.x>
- Key, R. M., Kozyr, A., Sabine, C. L., Lee, K., Wanninkhof, R., Bullister, J. L., ... Peng, T.-H. (2004). A global ocean carbon climatology: Results from Global Data Analysis Project (GLODAP). *Global Biogeochemical Cycles*, 18, GB4031. <https://doi.org/10.1029/2004GB002247>
- Kock, A., Arévalo-Martínez, D. L., Löscher, C. R., & Bange, H. W. (2016). Extreme N₂O accumulation in the coastal oxygen minimum zone off Peru. *Biogeosciences*, 13(3), 827–840. <https://doi.org/10.5194/bg-13-827-2016>
- Kock, A., & Bange, H. W. (2015). Counting the ocean's greenhouse gas emissions. *Eos*, 96(3), 10–13. <https://doi.org/10.1029/2015EO023665>
- Law, C. S., & Ling, R. D. (2001). Nitrous oxide flux and response to increased iron availability in the Antarctic Circumpolar Current. *Deep Sea Research Part II: Topical Studies in Oceanography*, 48(11–12), 2509–2527. [https://doi.org/10.1016/S0967-0645\(01\)00006-6](https://doi.org/10.1016/S0967-0645(01)00006-6), the Southern Ocean Iron Release Experiment (SOIREE).
- Law, C. S., & Owens, N. J. P. (1990). Significant flux of atmospheric nitrous oxide from the northwest Indian Ocean. *Nature*, 346(6287), 826–828. <https://doi.org/10.1038/346826a0>
- Li, C., von Storch, J.-S., & Marotzke, J. (2013). Deep-ocean heat uptake and equilibrium climate response. *Climate Dynamics*, 40(5), 1071–1086. <https://doi.org/10.1007/s00382-012-1350-z>
- Loescher, C. R., Kock, A., Koenneke, M., Laroche, J., Bange, H. W., & Schmitz, R. A. (2012). Production of oceanic nitrous oxide by ammonia-oxidizing archaea. *Biogeosciences*, 9(7), 2419–2429. <https://doi.org/10.5194/bg-9-2419-2012>
- Martin, J. H., Knauer, G. A., Karl, D. M., & Broenkow, W. (1987). VERTEX: Carbon cycling in the northeast Pacific. *Deep-Sea Research*, 34, 267–285. [https://doi.org/10.1016/0198-0149\(87\)90086-0](https://doi.org/10.1016/0198-0149(87)90086-0)
- Martínez-Rey, J., Bopp, L., Gehlen, M., Tagliabue, A., & Gruber, N. (2015). Projections of oceanic N₂O emissions in the 21st century using the IPSL Earth system model. *Biogeosciences*, 12(13), 4133–4148. <https://doi.org/10.5194/bg-12-4133-2015>
- McKay, M. D., Beckman, R. J., & Conover, W. J. (1979). A comparison of three methods for selecting values of input variables in the analysis of output from a computer code. *Technometrics*, 21, 239–245.
- Meinshausen, M., Smith, S., Calvin, K., Daniel, J., Kainuma, M., Lamarque, J.-F., ... van Vuuren, D. P. (2011). The RCP greenhouse gas concentrations and their extensions from 1765 to 2300. *Climatic Change*, 109(1), 213–241. <https://doi.org/10.1007/s10584-011-0156-z>
- Morell, J. M., Capella, J., Mercado, A., Bauzá, J., & Corredor, J. E. (2001). Nitrous oxide fluxes in Caribbean and tropical Atlantic waters: Evidence for near surface production. *Marine Chemistry*, 74(2–3), 131–143. [https://doi.org/10.1016/S0304-4203\(01\)00011-1](https://doi.org/10.1016/S0304-4203(01)00011-1)
- Müller, S. A., Joos, F., Edwards, N. R., & Stocker, T. F. (2006). Water mass distribution and ventilation time scales in a cost-efficient, three-dimensional ocean model. *Journal of Climate*, 19(21), 5479–5499. <https://doi.org/10.1175/JCLI3911.1>
- Müller, S. A., Joos, F., Edwards, N. R., & Stocker, T. F. (2008). Modeled natural and excess radiocarbon: Sensitivities to the gas exchange formulation and ocean transport strength. *Global Biogeochemical Cycles*, 22, GB3011. <https://doi.org/10.1029/2007GB003065>
- Najjar, R. G., Orr, J., Sabine, C. L., & Joos, F. (1999). Biotic-HOWTO. Internal OCMIIP Report (Tech. Rep.) Gif-sur-Yvette, France: LSCE/CEA Saclay.
- Naqvi, S. W. A., Jayakumar, D. A., Narvekar, P. V., Naik, H., Sarma, V. V. S. S., D'Souza, W., ... George, M. D. (2000). Increased marine production of N₂O due to intensifying anoxia on the Indian continental shelf. *Nature*, 408(6810), 346–349. <https://doi.org/10.1038/35042551>

- Nevison, C. (2003). Global distribution of N_2O and the ΔN_2O -AOU yield in the subsurface ocean. *Global Biogeochemical Cycles*, 17(4), 1119. <https://doi.org/10.1029/2003GB002068>
- Nevison, C. D., Weiss, R. F., & Erickson, D. J., III (1995). Global oceanic emissions of nitrous oxide. *Journal of Geophysical Research*, 100(C8), 15,809–15,820. <https://doi.org/10.1029/95JC00684>
- Nicholls, J. C., Davies, C. A., & Trimmer, M. (2007). High-resolution profiles and nitrogen isotope tracing reveal a dominant source of nitrous oxide and multiple pathways of nitrogen gas formation in the central Arabian Sea. *Limnology and Oceanography*, 52(1), 156–168. <https://doi.org/10.4319/lo.2007.52.1.0156>
- Orr, J., & Najjar, R. G. (1999). Abiotic-HOWTO. Internal OCMIP Report (Tech. Rep.) Gif-sur-Yvette, France: LSCE/CEA Saclay.
- Orr, J. C., & Epitalon, J.-M. (2015). Improved routines to model the ocean carbonate system: Mocsy 2.0. *Geoscientific Model Development*, 8(3), 485–499. <https://doi.org/10.5194/gmd-8-485-2015>
- Parekh, P., Joos, F., & Müller, S. A. (2008). A modeling assessment of the interplay between aeolian iron fluxes and iron-binding ligands in controlling carbon dioxide fluctuations during Antarctic warm events. *Paleoceanography*, 23, PA4202. <https://doi.org/10.1029/2007PA001531>
- Paulmier, A., Kriest, I., & Oschlies, A. (2009). Stoichiometries of remineralisation and denitrification in global biogeochemical ocean models. *Biogeosciences*, 6, 923–935.
- Peng, X., Fuchsman, C. A., Jayakumar, A., Oleynik, S., Martens-Habbena, W., Devol, A. H., & Ward, B. B. (2015). Ammonia and nitrite oxidation in the Eastern Tropical North Pacific. *Global Biogeochemical Cycles*, 29, 2034–2049. <https://doi.org/10.1002/2015GB005278>
- Popp, B. N., Westley, M. B., Toyoda, S., Miwa, T., Dore, J. E., Yoshida, N., ... Ostrom, P. H. (2002). Nitrogen and oxygen isotopomeric constraints on the origins and sea-to-air flux of N_2O in the oligotrophic subtropical North Pacific gyre. *Global Biogeochemical Cycles*, 16(4), 1064. <https://doi.org/10.1029/2001GB001806>
- Prather, M. J., Hsu, J., DeLuca, N. M., Jackman, C. H., Oman, L. D., Douglass, A. R., ... Funke, B. (2015). Measuring and modeling the lifetime of nitrous oxide including its variability. *Journal of Geophysical Research: Atmospheres*, 120, 5693–5705. <https://doi.org/10.1002/2015JD023267>
- Redfield, A. C., Ketchum, B. H., & Richards, F. A. (1963). The influence of organisms on the composition of sea-water. In M. N. Hill (Ed.), *The composition of seawater: Comparative and descriptive oceanography. The sea: Ideas and observations on progress in the study of the seas* (Vol. 2, pp. 26–77).
- Rees, A. P., Brown, I. J., Jayakumar, A., & Ward, B. B. (2016). The inhibition of N_2O production by ocean acidification in cold temperate and polar waters. *Deep Sea Research Part II: Topical Studies in Oceanography*, 127, 93–101. <https://doi.org/10.1016/j.dsr2.2015.12.006>
- Ritz, S. P., Stocker, T. F., & Joos, F. (2011). A coupled dynamical ocean-energy balance atmosphere model for paleoclimate studies. *Journal of Climate*, 24(2), 349–375. <https://doi.org/10.1175/2010JCLI3351.1>
- Roth, R. (2013). Modeling forcings and responses in the global carbon cycle-climate system: Past, present and future (PhD thesis). Climate and Environmental Physics, Bern, Switzerland: University of Bern.
- Roth, R., Ritz, S. P., & Joos, F. (2014). Burial-nutrient feedbacks amplify the sensitivity of carbon dioxide to changes in organic matter remineralisation. *Earth System Dynamics*, 5(1), 321–343. <https://doi.org/10.5194/esdd-5-473-2014>
- Saikawa, E., Prinn, R. G., Dlugokencky, E., Ishijima, K., Dutton, G. S., Hall, B. D., ... Elkins, J. W. (2014). Global and regional emissions estimates for N_2O . *Atmospheric Chemistry and Physics*, 14(9), 4617–4641. <https://doi.org/10.5194/acp-14-4617-2014>
- Santoro, A. E., Buchwald, C., McIlvin, M. R., & Casciotti, K. L. (2011). Isotopic signature of N_2O produced by marine ammonia-oxidizing archaea. *Science*, 333(6047), 1282–1285. <https://doi.org/10.1126/science.1208239>
- Sarmiento, J. L., & Gruber, N. (2006). *Ocean biogeochemical dynamics* (pp. 318–358). Princeton, NJ: Princeton University Press.
- Schilt, A., Baumgartner, M., Blunier, T., Schwander, J., Spahni, R., Fischer, H., & Stocker, T. F. (2010). Glacial-interglacial and millennial-scale variations in the atmospheric nitrous oxide concentration during the last 800,000 years. *Quaternary Science Reviews*, 29(1–2), 182–192. <https://doi.org/10.1016/j.quascirev.2009.03.011>
- Schilt, A., Brook, E. J., Bauska, T. K., Baggenstos, D., Fischer, H., Joos, F., ... Stocker, T. F. (2014). Isotopic constraints on marine and terrestrial N_2O emissions during the last deglaciation. *Nature*, 516(7530), 234–237. <https://doi.org/10.1038/nature13971>
- Schmidtko, S., Stramma, L., & Visbeck, M. (2017). Decline in global oceanic oxygen content during the past five decades. *Nature*, 542(7641), 335–339. <https://doi.org/10.1038/nature21399>
- Schmittner, A., & Galbraith, E. D. (2008). Glacial greenhouse-gas fluctuations controlled by ocean circulation changes. *Nature*, 456(7220), 373–6. <https://doi.org/10.1038/nature07531>
- Schmittner, A., Oschlies, A., Matthews, H. D., & Galbraith, E. D. (2008). Future changes in climate, ocean circulation, ecosystems, and biogeochemical cycling simulated for a business-as-usual CO_2 emission scenario until year 4000 AD. *Global Biogeochemical Cycles*, 22, GB1013. <https://doi.org/10.1029/2007GB002953>
- Schmittner, A., Urban, N. M., Keller, K., & Matthews, D. (2009). Using tracer observations to reduce the uncertainty of ocean diapycnal mixing and climate-carbon cycle projections. *Global Biogeochemical Cycles*, 23, GB4009. <https://doi.org/10.1029/2008GB003421>
- Steinacher, M., & Joos, F. (2016). Transient Earth system responses to cumulative carbon dioxide emissions: Linearities, uncertainties, and probabilities in an observation-constrained model ensemble. *Biogeosciences*, 13(4), 1071–1103. <https://doi.org/10.5194/bg-13-1071-2016>
- Steinacher, M., Joos, F., Bopp, L., Cadule, P., Doney, S. C., Gehlen, M., ... Segschneider, J. (2009). Projected 21st century decrease in marine productivity: A multi-model analysis. *Biogeosciences*, 7, 7933–7981.
- Steinacher, M., Joos, F., & Stocker, T. F. (2013). Allowable carbon emissions lowered by multiple climate targets. *Nature*, 499, 197–201. <https://doi.org/10.1038/nature12269>
- Stocker, B. D., Roth, R., Joos, F., Spahni, R., Steinacher, M., Zaehle, S., ... Prentice, I. C. (2013). Multiple greenhouse-gas feedbacks from the land biosphere under future climate change scenarios. *Nature Climate Change*, 3(7), 666–672.
- Stocker, T., Qin, D., Plattner, G.-K., Alexander, L., Allen, S., Bindoff, N., ... Xie, S.-P. (2013). Technical summary. In T. Stocker, et al. (Eds.), *Climate change 2013 the physical science basis. Contribution of working group I to the fifth assessment report of the intergovernmental panel on climate change*. Cambridge, United Kingdom and New York, NY: Cambridge University Press. <https://doi.org/10.1017/CBO9781107415324.004>
- Suntharalingam, P., & Sarmiento, J. L. (2000). Factors governing the oceanic nitrous oxide distribution: Simulations with an ocean general circulation model. *Global Biogeochemical Cycles*, 14(1), 429–454. <https://doi.org/10.1029/1999GB900032>
- Suntharalingam, P., Sarmiento, J. L., & Toggweiler, J. R. (2000). Global significance of nitrous-oxide production and transport from oceanic low-oxygen zones: A modeling study. *Global Biogeochemical Cycles*, 14(4), 1353–1370. <https://doi.org/10.1029/1999GB900100>
- Thompson, R. L., Chevallier, F., Crotwell, A. M., Dutton, G., Langenfelds, R. L., Prinn, R. G., ... Aoki, S. (2014). Nitrous oxide emissions 1999 to 2009 from a global atmospheric inversion. *Atmospheric Chemistry and Physics*, 14(4), 1801–1817. <https://doi.org/10.5194/acp-14-1801-2014>

- Trimmer, M., Chronopoulou, P. M., Maanoja, S. T., Upstill-Goddard, R. C., Kitidis, V., & Purdy, K. J. (2016). Nitrous oxide as a function of oxygen and archaeal gene abundance in the North Pacific. *Nature Communications*, 7, 13451. <https://doi.org/10.1038/ncomms13451>
- Tschumi, T., Joos, F., Gehlen, M., & Heinze, C. (2011). Deep ocean ventilation, carbon isotopes, marine sedimentation and the deglacial CO₂ rise. *Climate of the Past*, 7(3), 771–800. <https://doi.org/10.5194/cp-7-771-2011>
- Wanninkhof, R. (1992). Relationship between wind speed and gas exchange over the ocean. *Journal of Geophysical Research*, 97(C5), 7373–7382. <https://doi.org/10.1029/92JC00188>
- Ward, B. B. (2008). Chapter 5: Nitrification in marine systems. In D. G. Capone, et al. (Eds.), *Nitrogen in the marine environment* (2nd ed., pp. 199–261). San Diego, CA: Academic Press. <https://doi.org/10.1016/B978-0-12-372522-6.00005-0>
- Weaver, A. J., Sedláček, J., Eby, M., Alexander, K., Crespín, E., Fichefet, T., ... Zickfeld, K. (2012). Stability of the Atlantic meridional overturning circulation: A model intercomparison. *Geophysical Research Letters*, 39, L20709. <https://doi.org/10.1029/2012GL053763>
- Wilson, S. T., del Valle, D. A., Segura-Noguera, M., & Karl, D. M. (2014). A role for nitrite in the production of nitrous oxide in the lower euphotic zone of the oligotrophic North Pacific Ocean. *Deep Sea Research Part I: Oceanographic Research Papers*, 85, 47–55. <https://doi.org/10.1016/j.dsr.2013.11.008>
- Yamagishi, H., Westley, M. B., Popp, B. N., Toyoda, S., Yoshida, N., Watanabe, S., ... Yamanaka, Y. (2007). Role of nitrification and denitrification on the nitrous oxide cycle in the eastern tropical North Pacific and Gulf of California. *Journal of Geophysical Research*, 112, G02015. <https://doi.org/10.1029/2006JG000227>
- Yamamoto, A., Abe-Ouchi, A., Shigemitsu, M., Oka, A., Takahashi, K., Ohgaito, R., & Yamanaka, Y. (2015). Global deep ocean oxygenation by enhanced ventilation in the Southern Ocean under long-term global warming. *Global Biogeochemical Cycles*, 29, 1801–1815. <https://doi.org/10.1002/2015GB005181>
- Yang, S., & Gruber, N. (2016). The anthropogenic perturbation of the marine nitrogen cycle by atmospheric deposition: Nitrogen cycle feedbacks and the 15N Haber-Bosch effect. *Global Biogeochemical Cycles*, 30, 1418–1440. <https://doi.org/10.1002/2016GB005421>
- Yool, A., Martin, A. P., Fernández, C., & Clark, D. R. (2007). The significance of nitrification for oceanic new production. *Nature*, 447(7147), 999–1002. <https://doi.org/10.1038/nature05885>
- Zamora, L. M., & Oschlies, A. (2014). Surface nitrification: A major uncertainty in marine N₂O emissions. *Geophysical Research Letters*, 41, 4247–4253. <https://doi.org/10.1002/2014GL060556>
- Zamora, L. M., Oschlies, A., Bange, H. W., Huebert, K. B., Craig, J. D., Kock, A., & Löscher, C. R. (2012). Nitrous oxide dynamics in low oxygen regions of the Pacific: Insights from the MEMENTO database. *Biogeosciences*, 9(12), 5007–5022. <https://doi.org/10.5194/bg-9-5007-2012>
- Zhu-Barker, X., Cavazos, A. R., Ostrom, N. E., Horwath, W. R., & Glass, J. B. (2015). The importance of abiotic reactions for nitrous oxide production. *Biogeochemistry*, 126(3), 251–267. <https://doi.org/10.1007/s10533-015-0166-4>
- Zickfeld, K., Eby, M., Weaver, A. J., Alexander, K., Crespín, E., Edwards, N. R., ... Zhao, F. (2013). Long-term climate change commitment and reversibility: An EMIC intercomparison. *Journal of Climate*, 26(16), 5782–5809. <https://doi.org/10.1175/JCLI-D-12-00584.1>